INVESTIGATING ALBEDO AND PRECIPITATION SUSCEPTIBILITY OF

MARINE BOUNDARY LAYER CLOUDS USING

A-TRAIN DATA

by

Trevor James Ferguson

A thesis submitted to the faculty of
The University of Utah
in partial fulfillment of the requirements for the degree of

Master of Science

Department of Atmospheric Sciences

The University of Utah

December 2014

The University of Utah Graduate School

STATEMENT OF THESIS APPROVAL

The thesis of **Trevor James Ferguson**

has been approved by the following supervisory committee members:

Gerald G. Mace	, Chair	**07/22/2014**	
		Date Approved	
Timothy J. Garrett	, Member	**07/22/2014**	
		Date Approved	
Steven K. Krueger	, Member	**07/22/2014**	
		Date Approved	

and by **Kevin D. Perry** , Chair/Dean of

the Department/College/School of **Atmospheric Sciences**

and by David B. Kieda, Dean of The Graduate School.

ABSTRACT

Marine boundary layer clouds are an important component of Earth's climate system due to their vast spatial and temporal coverage. Representation of these clouds in climate models remains challenging and continues to result in the largest feedback uncertainties. It is essential to increase understanding of cloud physical processes in order to improve climate models. In this study, we investigate possible conditions influencing albedo and precipitation susceptibility of marine boundary layer clouds, which gauge the clouds' sensitivity to perturbations in aerosol concentration. To do so, we employ a recently developed retrieval algorithm that uses A-Train satellite data to infer cloud properties. This unique algorithm assumes a bimodal particle size distribution, and then uses information from CloudSat and MODIS to simultaneously retrieve cloud mode and precipitation mode properties. Additionally, a new parameterization for the single scattering properties of clouds is developed to account for the bimodal size distribution, and is used to help provide constraints for the cloud retrieval. An equivalent retrieval has been developed to use ground-based ARM data. To study marine boundary layer cloud susceptibility, we focus our attention on the region spanning the stratocumulus cloud regime near California and the trade cumulus cloud regime near Hawaii. We compare albedo and precipitation susceptibility between winter and summer months and also between high and low surface wind conditions. It is found that cloud droplet number concentrations vary between seasons and surface wind

conditions. Albedo susceptibility tends to increase monotonically with liquid water path (LWP). Precipitation susceptibility, on the other hand, shows non-monotonic behavior characterized by an autoconversion regime at low LWP and a transition to an accretion regime at higher LWP.

TABLE OF CONTENTS

CHAPTER 1

INTRODUCTION

1.1 Importance of Marine Boundary Layer Clouds

Marine boundary layer clouds form an important component of Earth's climate

system (Paluch and Lenschow 1991, Klein and Hartmann 1993, Norris 1998, Stevens et

al. 2003, Lin et al. 2009, Wood 2012). Specifically, their large spatial coverage,

persistence, and high albedo reduce the amount of incoming solar radiation received at

the surface, exerting a cooling effect on the Earth (Hartmann et al. 1992, Bretherton et al.

2004, Xu et al. 2005, Lin et al. 2009, Myers and Norris 2013). In the current climate, the

net global mean cloud radiative effect (includes all cloud types) is approximately -20 W

m^{-2} (Boucher et al. 2013). This net negative radiative effect due to clouds can be

attributed mainly to the extensive marine stratus and stratocumulus cloud decks which

persist over eastern subtropical oceans (Hartmann et al. 1992, Bretherton and Hartmann

2009, Boucher et al. 2013). Because of this, the sensitivity of these clouds to small

perturbations in environmental conditions has the potential to substantially influence

climate (Lohmann 2009, Stevens et al. 2003, Mauger and Norris 2010). Consequently, it

is important to understand the physical processes that govern these clouds in order to

determine cloud responses to a changing climate.

Yet marine boundary layer clouds seem to dominate tropical cloud feedback

uncertainties in climate models (Bony and Dufresne 2005, Soden and Vecchi 2011,

Brient and Bony 2012). According to the Intergovernmental Panel on Climate Change Fifth Assessment Report (IPCC AR5), low-cloud feedback ranges from -0.09 to +0.63 W m^{-2} $°C^{-1}$ among Cloud Feedback Model Intercomparison Project (CFMIP) global circulation models, and positive values are largely associated with a reduction in low-cloud amount in a warming in climate (Boucher et al. 2013). Along those lines, Soden and Vecchi (2011) suggest that changes in low-cloud amount are the primary driver for intermodel spread in cloud feedback. Furthermore, Bony and Dufresne (2005) advocate that the simulation of the sensitivity of these clouds to changing environmental conditions constitutes further uncertainty.

With that in mind, marine boundary layer clouds are difficult to accurately represent in climate models (Randall et al. 2003, Stevens et al. 2005). First, the complex interaction of these clouds with the marine boundary layer, coupled by radiative, microphysical, and dynamical processes, complicates their representation in numerical models (Kollias et al. 2004, Lin et al. 2009, Lohmann 2009, Boucher et al. 2013). Such processes range from cloud droplet growth to large-scale atmospheric dynamics such as subsidence. In addition, the fundamental details governing marine boundary layer clouds are not completely understood (Bony et al. 2006, Boucher et al. 2013).

Second, because general circulation models (GCMs) operate at large grid sizes, the smaller scale cloud processes must be parameterized (Randall et al. 2003, Boucher et al. 2013). By definition, a parameterization represents the effects of the small-scale processes in terms of the large-scale state (Randall et al. 2003). Parameterizations of boundary layer turbulence, convection, cloud microphysical processes, radiative transfer, and the resulting cloud amount must work in unison to simulate clouds in climate models

(Wyant et al. 2009, Boucher et al. 2013, Flato et al. 2013). However, Stephens (2005) states that aspects of these parameterizations remain worrisome, containing levels of empiricism and assumptions that are hard to evaluate with current global observations. Thus, uncertainties in cloud parameterizations are a major factor in the overall uncertainty in climate model projections (Wyant et al. 2009).

1.2 Marine Stratocumulus

The environment of marine stratocumulus clouds is typically characterized by a shallow, well-mixed marine boundary layer, cool sea surface temperatures (SST), and strong lower tropospheric stability and temperature inversion associated with large-scale subsidence of the descending branch of the Hadley circulation (Albrecht et al. 1988, Paluch and Lenschow 1991, Kollias et al. 2004, Myers and Norris 2013). Lower tropospheric stability (LTS) is defined as the difference between the potential temperature θ of the free troposphere (700 hPa) and the surface (Wood and Bretherton 2006),

$$LTS = \theta_{700} - \theta_0. \tag{1}$$

Klein and Hartmann (1993) found that seasonal variations of marine low-cloud amount are well correlated with seasonal mean LTS, with summer months exhibiting higher LTS and hence greater cloud amount. Indeed, high LTS and a strong low-lying temperature inversion both promote a well-mixed boundary layer by coupling the stratocumulus cloud layer to the surface moisture supply and limiting cloud top entrainment (Bretherton and Wyant 1997, Wyant et al. 1997, Wood and Bretherton 2006, Bretherton and Hartmann 2009).

With that in mind, LTS is strongly correlated to SST and the free-tropospheric temperature (Wood 2012). Therefore, cooler SSTs combined with large-scale subsidence of warm, dry air aloft generates an environment of strong LTS. This creates conditions for a temperature inversion above the boundary layer, which is essential for the formation of marine stratiform cloud decks (Paluch and Lenschow 1991). As a result, the cloud layer is confined to the boundary layer and is more easily coupled to the ocean moisture source, which helps maintain the cloud.

Once the cloud has formed, strong longwave cooling at cloud top drives convective instability which helps to 1) promote the temperature inversion immediately above the cloud top, 2) maintain a well-mixed boundary layer via the production of large buoyancy fluxes, and 3) couple the cloud layer to the ocean surface moisture supply (Wood 2012). As the cloud top cools, the affected parcels of air become negatively buoyant, resulting in downdrafts within the cloud, which penetrate to the surface in a mixed layer. In the meantime, latent heat release at cloud base via condensation results in the updraft of warm, moist air. This differential heating drives convection (Wallace and Hobbs 2006), which is necessary for the preservation of the marine stratocumulus clouds (Wood 2012).

Large eddies within the cloud topped boundary layer can drive and enhance the entrainment of warm, dry free tropospheric air into the cloud layer (Wood 2012). Stronger turbulence associated with more energetic buoyancy fluxes will increase the rate of entrainment (Wallace and Hobbs 2006). Entrained air acts to evaporate cloud water, resulting in a parcel of air that is cooled and dried, which can be negatively buoyant (Wallace and Hobbs 2006). With that in mind, entrainment tends to deepen the boundary layer (Bretherton and Hartmann 2009) and thin the stratocumulus cloud layer by raising

the lifting condensation level faster than it raises the top of the boundary layer, processes which may lead to cloud dissipations (Wood 2012).

1.3 Stratocumulus-to-Cumulus Transition

Marine stratocumuli tend to exist in vast semipermanent cloud sheets over eastern subtropical ocean basins near the west coasts of North and South America and the Southern part of the African continent (Klein and Hartmann 1993, Martin et al. 1995, Wood 2012). Moving westward and equatorward, the cloud regime changes from stratocumulus to trade wind cumulus. As an example, Figure 1 shows a MODIS satellite image of the stratocumulus cloud regime near California, and the trade cumulus regime near Hawaii. This transition is climatologically important to consider (Albrecht et al. 1995, Xiao et al. 2010) since there is a substantial contrast in cloud radiative forcing between these two cloud regimes due to differences in cloud cover (Karlsson et al. 2010). Hence, it is important to understand the factors regulating this transition in order to provide proper parameterizations of marine boundary layer clouds in climate models (Wang and Lenschow 1995).

Decoupling of the boundary layer (i.e., a separation of the cloud layer from the surface moisture supply) is a crucial step in the stratocumulus-to-cumulus transition (Bretherton and Wyant 1997). Recall that cool sea surface temperatures and high LTS characterize the stratocumulus regime. When the air mass associated with this regime is advected equatorward with the trade winds, it is exposed to warmer sea surface temperatures as well as weakening subsidence (Karlsson et al. 2010), resulting in decreased LTS and dramatically increased surface latent heat fluxes (Wyant et al. 1997, Wood 2012). Consequently, the boundary layer begins to deepen due to increased

Figure 1. MODIS image of the eastern subtropical Pacific Ocean with vast stratocumulus cloud sheets near the California coast and patchy trade cumulus near Hawaii. Notice the difference in cloud cover between the two cloud regimes. (Image courtesy of NASA).

surface buoyancy fluxes (Krueger et al. 1995), which increases buoyancy fluxes and turbulence levels within the cloud and enhances entrainment at cloud top (Wyant et al. 1997, Sandu et al. 2010). When the boundary layer deepens beyond 1 km, it becomes increasingly difficult for longwave cooling at cloud top to sustain mixing of the positively buoyant entrained air over the entire depth of the boundary layer (Bretherton and Wyant 1997, Wood 2012). As a result, a weakly stable transition layer begins to form below cloud base due to increased negative buoyancy fluxes below cloud base associated with the downward flux of warm entrained air (Wyant et al. 1997). Accordingly, the stable layer separates the surface mixed layer from the cloud layer (Wang and Lenschow 1995, Wyant et al. 1997, Karlsson et al. 2010), cutting off the surface moisture supply to the cloud and preventing negatively buoyant eddies generated by cloud top longwave cooling from mixing through the subcloud layer (Wood 2012). Eventually, the stratocumulus cloud layer begins to decouple from the surface mixed layer and may begin to thin and dissipate (Wood 2012).

In the meantime, surface fluxes of heat and moisture cause the relative humidity in the surface mixed layer to increase, and cumulus clouds begin to form when the surface mixed layer becomes conditionally unstable (Martin et al. 1995). Strong convective updrafts allow the cumuli to locally penetrate the weakly stable transition layer, which may initially help maintain the stratocumulus layer by venting in moisture from the surface (Johnson et al. 1994, Wang and Lenschow 1995, Wyant et al. 1997). However, as the cumuli become more vigorous, they increase the entrainment of dry air at cloud top, eventually leading to the thinning and dissipation of the stratocumulus cloud

layer, thus exposing the underlying cumulus (Sandu et al. 2010, Wood 2012). In summary, Figure 2 depicts this cloud transition process (Albrecht et al. 1995).

Other processes that may affect the marine boundary layer cloud transition include precipitation (Bretherton and Wyant 1997, Sandu and Stevens 2011, Wood 2012) and cloud absorption of solar radiation (Paluch et al. 1994, Bretherton and Wyant 1997, Wood 2012). Marine stratocumulus clouds often precipitate in the form of drizzle (Wood 2012). This has the effect of warming the cloud layer via latent heat release by the condensation of water vapor (Wallace and Hobbs 2006). As a result, turbulent mixing within the cloud decreases due to stabilization (Wood 2012). In addition, evaporation of drizzle below cloud base absorbs latent heat, and moistens and cools the subcloud layer, causing further stabilization and suppressing turbulence within the boundary layer (Paluch et al. 1994, Wallace and Hobbs 2006, Sandu and Stevens 2011). Consequently, cloud growth is inhibited (Wood 2012), cloud liquid water is depleted, and decoupling of the boundary layer may occur (Nicholls 1984, Albrecht 1989). However, Stevens et al. (1998) caution that drizzle should not necessarily be taken as a sign of decoupling. Furthermore, the cooling and moistening of the subcloud layer favors the formation of cumuli by promoting enhanced surface sensible heat fluxes (Feingold et al. 1996, Stevens et al. 1998, Sandu and Stevens 2011).

Similarly, cloud absorption of solar radiation acts to stabilize the boundary layer and suppress turbulence (Paluch et al. 1994). A diurnal decoupling of the boundary layer ensues and the cloud layer thins during the day (Bretherton and Wyant 1997). At night, the absence of the shortwave heating allows the cloud layer to revitalize (Wyant et al. 1997). However, if precipitation is present, it limits cloud reformation at night (Sandu
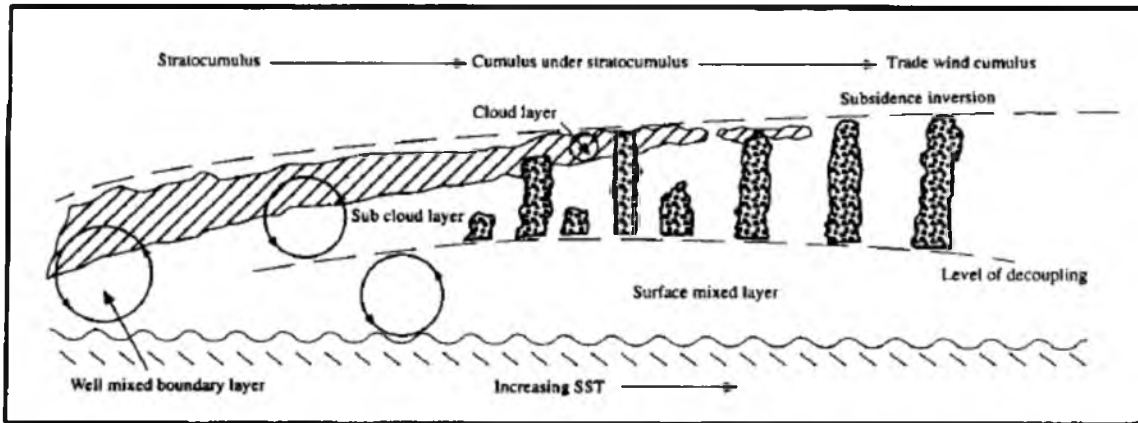
Figure 2. Depiction of marine stratocumulus-to-trade wind cumulus transition (reprinted from Albrecht et al. 1995, ©American Meteorological Society, used with permission).

and Stevens 2011).

Although precipitation and solar radiation influence the cloud-topped marine boundary layer, they do not regulate or control the stratocumulus-to-cumulus transition (Wyant et al. 1997, Stevens et al. 1998, Sandu and Stevens 2011). In fact, eddy-resolving simulations show that the transition occurs mainly as a function of increased latent heat fluxes as the air advects over progressively warmer sea surface temperatures (Albrecht et al. 1995, Wyant et al. 1997, Sandu and Stevens 2011). Precipitation and absorption of solar radiation may accelerate the transition in cloud fraction, but do not play a qualitative role in the cloud transition itself (Wyant et al. 1997, Sandu and Stevens 2011).

General circulation models (GCMs) continue to have difficulty in successfully representing the stratocumulus and trade cumulus marine boundary layer regimes and the transition between them (Siebesma et al. 2004, Xiao et al. 2010, Teixeira et al. 2011). As an example, Teixeira et al. (2011) analyzed a number of different weather and climate models along the stratocumulus-to-cumulus transition from California to the Intertropical Convergence Zone (ITCZ) (called the GPCI transect) and compared the results to the International Satellite Cloud Climatology Project (ISCCP) observations. They found that most of these models underestimated cloud amount in the stratocumulus regime, overestimated cloud amount in the cumulus regime, and produced a too early occurrence in the transition between the two cloud regimes. A similar study conducted by Siebesma et al. (2004) showed like results.

The problematic model results are largely due to an incomplete understanding of marine boundary layer processes involved in the transition, which frustrates advancements toward improved parameterizations (Xiao et al. 2010). Also, intermodel

differences arise as a result of various parameterizations used to represent marine boundary layer clouds in models (Siebesma et al. 2004, Teixeira et al. 2011). Furthermore, a lack of observational data to constrain and evaluate models limits further progress (Paluch et al. 1994, Lewis and Wiscombe 2012). Thus, efforts are continually being made to acquire observational data and to improve cloud parameterizations in models (Lewis and Wiscombe 2012).

With this purpose in mind, a recently completed field campaign funded by the US Department of Energy's Atmospheric Radiation Measurement (ARM) program deployed a mobile facility aboard the Horizon Lines cargo container ship merchant vessel (M/V) *Spirit* for the Marine ARM GPCI Investigation of Clouds (MAGIC) (http://www.arm.gov/sites/amf/mag/). The cargo ship regularly traverses the Pacific Ocean along a route from Los Angeles, CA, $(33.7°N, 118.3°W)$ to Honolulu, HI $(21.3°N, 157.9°W)$ as shown in Figure 3, making a complete round trip every two weeks. Specifically, the deployment ran from October 2012 to October 2013. One of the main objectives of the MAGIC field campaign is to produce high-resolution, intraseasonal observational data sets of marine boundary layer clouds in order to improve the representation of the stratocumulus-to-cumulus transition in climate models (Lewis and Wiscombe 2012). In our study, we will focus on the MAGIC transect region to investigate albedo and precipitation susceptibility of marine boundary layer clouds.

Figure 3. MAGIC transect. This route traverses the stratocumulus regime near California and the trade cumulus regime near Hawaii, making it an ideal location to study marine boundary layer clouds and the stratocumulus to cumulus transition. Note, the Hawaiian Islands are not to scale in either distance or size. (Image courtesy of ARM).

1.4 Cloud Droplet Growth

Clouds form when air becomes supersaturated with respect to liquid water (Twomey 1977, Wallace and Hobbs 2006). Supersaturation is a condition in which the relative humidity exceeds 100%. In the atmosphere, this condition most commonly occurs as a moist parcel of air rises, expands, and adiabatically cools (Wallace and Hobbs 2006). As it does so, the relative humidity increases and once supersaturation is reached, water vapor condenses onto some of the particles in the air to form a cloud of small water droplets.

Essential for cloud droplet formation is the presence of cloud condensation nuclei (CCN), which act to decrease the supersaturation needed for a cloud droplet to form (Houze 1993, Wallace and Hobbs 2006). Otherwise, in perfectly clean air without CCN, water droplets begin to condense only when the relative humidity reaches several hundred percent (Rogers and Yau 1989, Hobbs 1993). Fortunately, the atmosphere contains aerosols that act as CCN to nucleate cloud droplets and form clouds.

Once the cloud droplet has formed, it may begin to grow depending on whether there is sufficient ambient water vapor, otherwise it will evaporate (Rogers and Yau 1989). However, as long as the ambient vapor density is greater than the vapor density at the droplet's surface, the cloud droplet will grow (Rogers and Yau 1989). With that in mind, droplets can grow by condensation in a supersaturated environment and by colliding and coalescing with other cloud droplets (Wallace and Hobbs 2006). In the early development of a cloud, the droplets are too small for collision-coalescence to take effect (Rogers and Yau 1989). Therefore, growth by condensation initially dominates the cloud droplet development (Wallace and Hobbs 2006).

Droplet growth by condensation occurs through the diffusion of ambient water vapor onto the cloud droplet (Rogers and Yau 1989). During this process, the rate of the growth of the droplet radius is inversely proportional to the cloud droplet size (Rogers and Yau 1989, Wallace and Hobbs 2006). Accordingly, small droplets grow very rapidly. However, as the droplet increases in size, the growth rate eventually decreases. Once the droplet reaches about 20 μm to 30 μm in radius, collision-coalescence is likely to be the dominant growth process (Rogers and Yau 1989), in which large collector drops capture smaller cloud droplets. The number of collisions a collector drop experiences increases rapidly as the drop gets bigger in size, proportionate to the fourth power of the drop radius, so that coalescence proceeds at an accelerating pace once it begins (Rogers and Yau 1989). As the cloud drop grows, it becomes subject to gravitational forces and may leave the cloud and fall as precipitation.

1.5 Precipitation

The mechanism responsible for precipitation in marine boundary layer clouds is primarily coalescence among cloud droplets because growth by condensation alone to sizes larger than 20 μm takes too long to explain the observed precipitation growth in these clouds (Rogers and Yau 1989, Hobbs 1993, Jonas 1996, Wallace and Hobbs 2006, Wood 2012). As mentioned previously, marine boundary layer clouds often precipitate in the form of drizzle (Wood 2012), which by definition is a drop of water with a radius between 0.1 to 0.25 mm as opposed to a rain drop which has a typical radius of about 0.5 mm (Houze 1993). Leon et al. (2008) researched the climatology of drizzle in marine boundary layer clouds based on one year of data from the CloudSat and CALPISO

satellites and found drizzle to occur 19%-34% of the time in regions of persistent subtropical marine stratocumulus.

Drizzle in marine boundary layer clouds can greatly influence cloud albedo, lifetime, fractional coverage, and marine boundary layer structure (Albrecht 1989, Kostinski 2008, Savic-Jovcic and Stevens 2008, Suzuki and Stephens 2009). More specifically, by limiting cloud lifetime, drizzle can decrease average cloud fraction and, thus, cloud albedo (Albrecht 1989, Baker 1997, Kostinski 2008). This is because drizzle is the primary means of removing liquid water from the marine boundary layer that could otherwise condense into a cloud (Comstock et al. 2004, Lenderink and Siebesma 2004, Leon et al. 2008).

In the case of a weakly precipitating boundary layer when only small amounts of drizzle are produced, the evaporation of drizzle just below cloud base can destabilize the subcloud layer and enhance the mixing of moisture into the cloud, thus increasing cloudiness (Feingold et al. 2006, Ackerman et al. 2009, Stevens and Feingold 2009). On the other hand, stabilization of the subcloud layer results from evaporation of heavy drizzle throughout the subcloud layer, which leads to moisture accumulating in the surface layer (Paluch and Lenschow 1991, Ackerman et al. 2009). As a result, mixing between the cloud and subcloud layers is inhibited and a potential decoupling of the cloud layer from the surface may occur (Austin et al. 1995, Feingold et al. 1996, Stevens et al. 1998, Comstock et al. 2004, Leon et al. 2008), which can promote cloud breakup (Stevens et al. 1998, Comstock et al. 2005, Wood 2012).

Because of the mentioned influences drizzle has on marine boundary layer clouds, the processes by which cloud droplets grow and transition to precipitation, and their

representation in climate models, are fundamental in understanding cloud feedbacks in response to a changing climate (Bony and Dufresne 2005, Nakajima et al. 2010). With that in mind, numerical models represent the conversion of cloud water droplets to precipitation using parameterizations of two specific processes (Stephens and Haynes 2007). The first, called autoconversion, is the process whereby cloud droplets collide and coalesce to from drizzle drops (AMS Glossary of Meteorology). The second process is termed accretion and refers to the collection of cloud drops by colliding drizzle drops (AMS Glossary of Meteorology). Cloud amount and lifetime effects manifest themselves in GCMs by means of their representation of autoconversion and accretion (Boucher et al. 2013). Therefore, the manner in which parameterizations of these two processes are implemented in climate models can affect resulting cloud feedbacks.

CHAPTER 2

CLOUD-AEROSOL-PRECIPITATION-INTERACTION

2.1 Aerosol Indirect Effects

Previously mentioned was the importance of aerosols that act as CCN to activate

cloud droplet growth. This has important implications on cloud properties as the

background aerosol concentration, along with cloud-base vertical velocity, determines the

cloud droplet number concentration. Then, for a given cloud liquid water content, the

cloud droplet radius is regulated primarily by the cloud droplet number concentration

(Abdul-Razzak and Ghan 2000, Wood 2012). Much of a cloud's radiative properties are

dependent on the cloud droplet size, influencing the scattering and absorption of radiation

(Wood 2012). Furthermore, precipitation development depends on cloud droplet size as

discussed earlier. Thus, aerosol interaction with clouds and precipitation indirectly

influence Earth's climate and will be reviewed in this section.

It was proposed by Twomey (1977) that at a fixed cloud liquid water content, an

increase in CCN would act to increase cloud droplet number concentration and reduce the

cloud droplet size. Consequently, the cloud would have a higher albedo. This is

commonly known as the first aerosol indirect effect or the Twomey Effect. Guibert et al.

(2003) performed an observational study of the aerosol indirect effect in marine

stratocumulus clouds using data collected in 1997 from the second Aerosol

Characterization Experiment (ACE-2) conducted over the Atlantic Ocean near the Canary

Islands. They mention that cloud droplet number concentration varies with the origin of the air mass, from approximately 30 cm^{-3} in pristine marine air, to more than 1000 cm^{-3} in polluted regions. Also, when anthropogenic aerosol is added to the natural aerosol background, generally both the CCN and cloud droplet concentration increase (Guibert et al. 2003). Brenguier et al. (2000) also provide observational evidence that polluted clouds exhibit higher reflectance of radiation than in pristine marine clouds.

In addition to increasing cloud albedo, it has been suggested that changes in aerosol concentrations over the oceans may alter the amount of low-level cloudiness through a reduction in drizzle and a subsequent increase in cloud lifetime (Albrecht et al. 1989, Stevens and Feingold 2009). In essence, smaller cloud droplets in polluted clouds are less apt to initiate the collision-coalescence process and generate drizzle, thus reducing the cloud's ability to produce precipitation (Lohmann and Feichter 2005, Rotstayn and Liu 2005, Wang and Feingold 2009). Drizzle suppression, then, prevents the removal of cloud liquid water and prolongs cloud lifetime (Albrecht et al. 1989). This phenomenon is commonly referred to as the second aerosol indirect effect or the cloud lifetime effect. The distinguishing quality of this hypothesis is the idea that the macrostructure of the cloud (such as its liquid water content) is determined by the efficiency with which precipitation develops, which in turn is regulated in part by the aerosol (Stevens and Feingold 2009). Observations from the Tropical Rainfall Measuring Mission (TRMM) satellite validate this effect by demonstrating that smoke from burning vegetation can essentially shut off warm rain formation in tropical clouds (Rosenfeld 1999, Khain et al. 2000).

Recall that autoconversion is the dominant process determining cloud lifetime effects of aerosols in global climate models (Wang et al. 2012, Boucher et al. 2013). Autoconversion is sensitive to and inversely dependent on the cloud droplet number concentration (Feingold et al. 2013), and must be sufficiently active in order for warm clouds to precipitate (Wang et al. 2012). On the other hand, accretion is insensitive to the cloud droplet number concentration (Feingold et al. 2013), and the resulting precipitation rate is strongly dependent upon the accretion process (Wood 2005). Therefore, as Wang et al. (2012) state, the relative balance of autoconversion and accretion is critical for cloud lifetime effects of aerosols. With that in mind, the IPCC AR5 notes that GCMs tend to overestimate the magnitude of the aerosol effect on cloud properties because of a heavy reliance on the autoconversion rate, suggesting a too direct connection between the aerosol amount and cloud properties (Boucher et al. 2013). Indeed, cloud radiative forcings in GCMs have been found to be very sensitive to the autoconversion parameterization (Boucher et al. 2013).

2.2 Albedo Susceptibility

Albedo susceptibility is a concept used to better understand the first aerosol indirect effect on clouds. Specifically, it gauges the sensitivity of cloud albedo to perturbations in aerosol concentration. Platnick and Twomey (1994) define albedo susceptibility as

$$S = \frac{dA}{dN_d} \qquad (2)$$

which represents the change in albedo A to the change in cloud droplet number concentration N_d assuming a constant liquid water path. It is important to recall that N_d

is a function of the aerosol concentration. In their study, Platnick and Twomey (1994) used satellite cloud retrievals to compare the albedo susceptibility of ship track regions to out-of-track regions. In general, they found that clouds in the ship track regions had lower albedo susceptibility associated with higher cloud droplet number concentrations and smaller cloud droplet sizes. This would imply that the susceptibility has been realized, meaning that the clouds have already been perturbed and cannot be perturbed any further, thus the low susceptibility. Conversely, the out-of-track cloud regions contained more pristine air and hence smaller cloud droplet number concentrations, larger cloud droplet sizes, and resulting larger albedo susceptibility. In other words, clouds with high N_d are less sensitive to further perturbations in aerosol concentration whereas clouds in pristine environments characterized with low N_d are much more susceptible to changes in aerosol concentration.

Painemal and Minnis (2012) developed an alternative albedo susceptibility definition called the relative albedo susceptibility defined as

$$S_R = \frac{dA}{\frac{dN_d}{N_d}} = \frac{dA}{d \ln N_d}. \tag{3}$$

This is a useful metric as it takes into account the spatial variability and fractional changes in N_d. Furthermore, the authors point out that this definition ameliorates biases in N_d. For these reasons, we employ equation (3) in our study. All other references to albedo susceptibility throughout the remainder of this paper are in reference to this definition.

Taking the linear regression of A to $\ln N_d$ at a given liquid water path (LWP) gives the albedo susceptibility. From Painemal and Minnis (2012), the dependence of the cloud albedo A on N_d is expressed as

$$A = \alpha_{LWP} \cdot \ln(N_d) + \beta_{LWP} \qquad (4)$$

where α_{LWP} is the slope and β_{LWP} the intercept of the linear regression within a given LWP increment. Thus, the albedo susceptibility as defined in equation (3) can be rewritten as

$$S_R = \alpha_{LWP}. \qquad (5)$$

Using this method, Painemal and Minnis show that the linear relation between A and $\ln N_d$ yields correlation coefficients higher than 0.75.

With that in mind, Painemal and Minnis (2012) investigated the albedo susceptibility of offshore and coastal marine stratocumulus clouds for the climatologically significant stratocumulus regions near the SE Pacific, California, and Africa. Figure 4 shows the results from their study, with S_R values on the y-axis and LWP bins on the x-axis. For the coastal clouds, the albedo susceptibility initially increases linearly with LWP in all three regions. After reaching a maximum at a LWP near 50 g m^{-2}, the albedo susceptibility remains constant or slightly decreases. The offshore clouds, on the other hand, exhibit albedo susceptibility that linearly increases at all LWP values. To explain this, the authors suggest that the albedo susceptibility is modulated by changes in cloud optical thickness. Because of their proximity to abundant continental aerosol, the coastal clouds reach a greater optical thickness (and hence albedo) such that a peak in the albedo susceptibility is reached. Conversely, the offshore clouds reside in cleaner air such that the cloud optical depth remains smaller, and hence
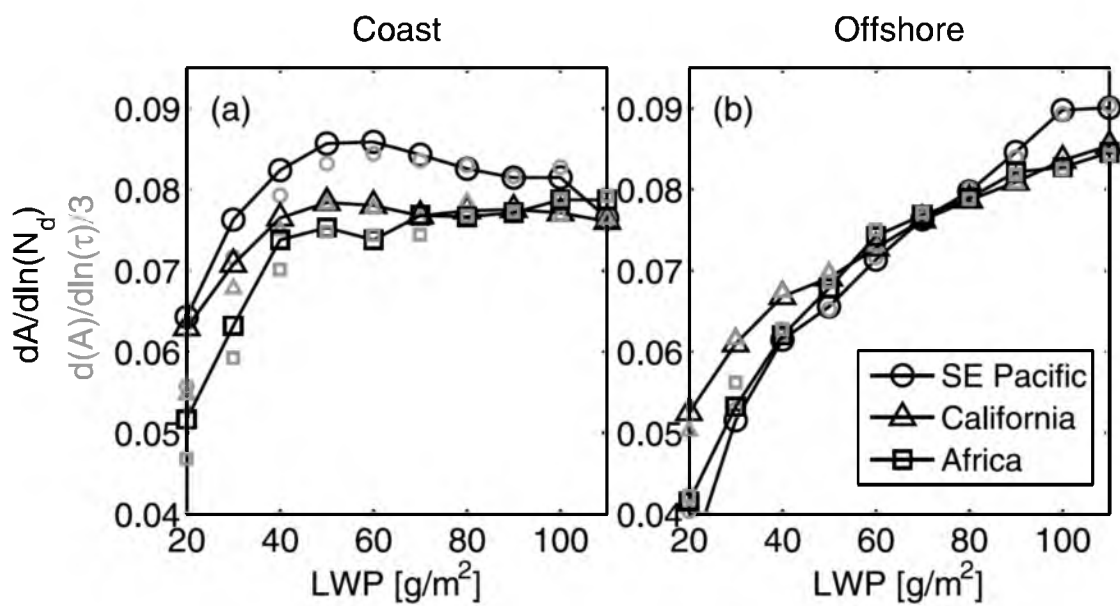
Figure 4. Relative albedo susceptibility S_R (black symbols) for coastal and offshore marine stratocumulus clouds (reprinted from Painemal and Minnis 2012, © 2012 by the American Geophysical Union, used with permission).

the albedo susceptibility continues to linearly increase with LWP. Naturally, clouds in a

pristine environment remain more susceptible to changes in cloud droplet number

concentration.

2.3 Precipitation Susceptibility

An analogous concept is precipitation susceptibility, which gauges the sensitivity

of precipitation to changes in cloud droplet number concentration (second aerosol

indirect effect). It can be used to identify which cloud types are most susceptible to

aerosol influences (Sorooshian et al. 2009). It is mathematically defined as

$$S_o = -\frac{d \ln R}{d \ln N_d} \qquad (6)$$

where R is the precipitation rate (Sorooshian et al. 2009). The minus sign is indicative of

the fact that precipitation rate is inversely proportional to the cloud droplet number

concentration. For instance, a small cloud droplet number concentration would entail a

higher sensitivity of precipitation to changes in aerosol concentration at a given

precipitation rate.

Similar to albedo susceptibility, precipitation susceptibility is calculated by taking

the linear regression of the two variables of interest, in this case $\ln R$ to $\ln N_d$, at fixed

LWP intervals. Figure 5 gives an example of S_o at various LWP values (Sorooshian et

al. 2009). Based upon this figure, the authors suggest three different susceptibility

regimes. The first occurs at low LWP wherein the precipitation susceptibility of the

cloud is small due to the fact that there is not enough liquid water to generate

precipitation. The second regime occurs at intermediate values of LWP where the cloud

is most susceptible to aerosol perturbations. The third regime occurs at high LWP values
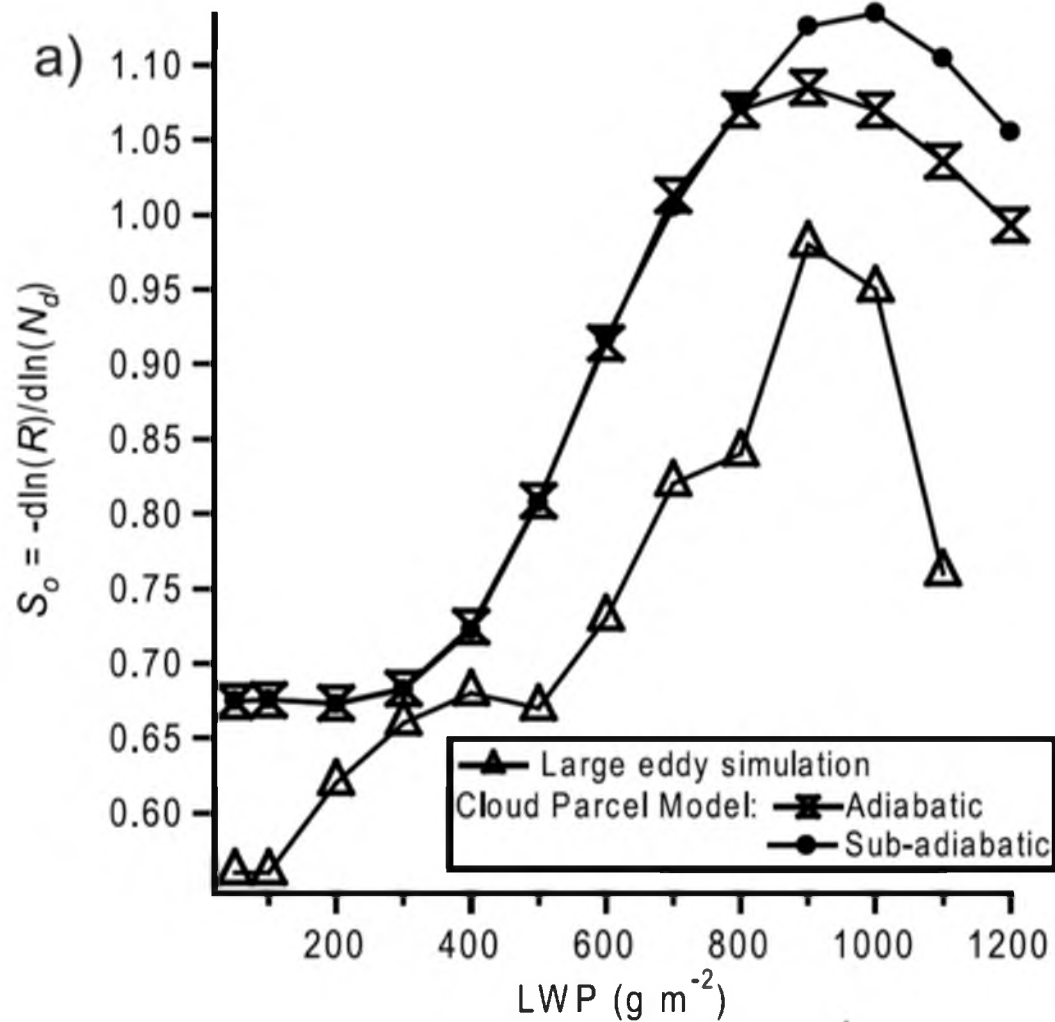
Figure 5. Precipitation susceptibility (reprinted from Sorooshian et al. 2009, © 2009 by the American Geophysical Union, used with permission).

in which the precipitation process is already sufficient, thus rendering any additional aerosol perturbation to have no effect on the precipitation process.

Recent observational and modeling studies have been performed to determine the controlling factors of precipitation susceptibility of warm clouds to changes in aerosol concentration (Sorooshian et al. 2009, Jiang et al. 2010, Feingold et al. 2013). It has been suggested that there exists a transition from an autoconversion regime to an accretion regime (Jiang et al. 2010, Feingold et al. 2013). Environments dominated by autoconversion are very susceptible to aerosol perturbations while environments dominated by accretion exhibit lower sensitivity to these perturbations. This is manifested by the non-monotonic nature of the precipitation susceptibility as shown in Figure 5. Where this transition occurs between autoconversion and accretion (the inflection point in the graph) may be a factor of environmental conditions. For example, Feingold et al. (2013) suggest that the time available for collision-coalescence (t_c) plays an important role in determining whether rain production is dominated by accretion or autoconversion, and therefore the extent to which the clouds are likely to be susceptible to aerosol perturbations. Factors affecting t_c include aerosol concentration, cloud depth, and updraft velocity. Indeed, in their study, Feingold et al. (2013) show that the transition between autoconversion and accretion occurs at higher LWP given a greater aerosol concentration. In addition, they show that decreasing updraft velocity, which decreases the cloud droplet number concentration and allows precipitation formation at smaller LWP, shifts the inflection point to smaller LWP.

An additional study by Terai et al. (2012) investigated the precipitation susceptibility of marine stratocumulus as a function of cloud thickness. In particular,

they examine the precipitation susceptibility of all clouds, precipitating or not. By so doing they attempt to quantify the effects of aerosols on the mean precipitation rates of all clouds of a given thickness. As a result, they found that the precipitation susceptibility of marine stratocumulus clouds decreases with increasing cloud thickness. With that in mind, the study points out that precipitation rate increases strongly with cloud thickness, and that the ability of aerosols to suppress precipitation is stronger in clouds that produces only weak precipitation. Thus, they conclude that aerosols appear to have a larger effect on thinner clouds than they do on thicker clouds. Similar results were found when they examined precipitation susceptibility as a function of LWP, with susceptibility decreasing as LWP increased. In contrast, Sorooshian et al. (2009) found little change in the precipitation susceptibility at LWP values (0 to 250 g m^{-2}) compared to Terai et al. (2012), who suggested that this difference is attributable to whether or not nonprecipitating clouds are included in the susceptibility calculation. Lastly, Terai et al. (2012) suggest that for thinner clouds, the reduction in precipitation susceptibility with increasing cloud thickness can be understood as a transition from autoconversion-dominated precipitation to accretion-dominated precipitation.

Also important to consider is the susceptibility of aerosol concentrations to precipitation through wet scavenging (Wood 2006, Grandey et al. 2014). As stated by Wood (2006), the main loss mechanism of CCN in the marine boundary layer is through the process of cloud and drizzle drops coalescing with each other, wherein each coalescence event effectively removes a single CCN from the marine boundary layer. Thus, aerosol concentration can be regulated by precipitation variability, which in turn may influence the precipitation susceptibility of the cloud. Indeed, Wood (2006) found

that a precipitation rate as little as 1 mm d^{-1} is sufficient to drive down the CCN

concentration by a factor of three over the remote ocean. In addition, Grandey et al.

(2014) observed that wet scavenging of aerosols by precipitation leads to a negative

relationship between precipitation rate and aerosol concentration (i.e., as precipitation

rate increases, aerosol concentration decreases as a result of scavenging). Determining

the causality of whether precipitation susceptibility is driven by aerosol susceptibility to

precipitation or to environmental or meteorological conditions is a difficult task and

needs further study.

CHAPTER 3

DATA AND METHODS

3.1 A-Train

To reiterate, the objective of this study is to learn about the processes marine

boundary layer clouds go through in their lifecycles as well as what controls the rate at

which these processes happen. The albedo and precipitation susceptibility, then, are

concepts to help us gain this understanding. To do this, we employ satellite data from

NASA's A-Train, which is a constellation of satellites in close formation. The A-Train

stands for "afternoon train" since the satellites cross the equator around 1:30 PM local

time each day. This unique suite of instrumentation provides a synergistic view of

clouds. Specifically, data from the A-Train's CloudSat and Aqua are used in this study.

CloudSat was launched 28 April 2006 with the objective to provide the necessary

observations to advance understanding of cloud abundance, distribution, structure, and

radiative properties (Stephens et al. 2008). Onboard CloudSat is the Cloud Profiling

Radar (CPR), which operates at 94 GHz (~3 mm wavelength). It is a nadir pointing radar

with an along-track resolution of 1.7 km and a cross-track resolution of 1.4 km. The

minimum detectible signal is around -29 dBZ with a vertical range gate resolution of 480

m, which is determined by the pulse width. However, the data are oversampled to

produce 240 m range gate spacing. The CPR identifies significant radar echoes from

hydrometeors in order to provide radar reflectivity estimates, which are used for our study.

Aqua was launched 4 May 2002, making it the first satellite comprising the current A-Train constellation. The Moderate Resolution Imaging Spectroradiometer (MODIS) instrument onboard Aqua acquires data in thirty-six spectral bands ranging from 0.4 μm to 14.4 μm. In this study, we utilize measurements from the MODIS-AUX data product, which contains a subset of ancillary MODIS radiance and cloud mask data that overlaps and surrounds each CloudSat CPR footprint (Partain 2007). Specifically used are the 0.55 μm and 2.1 μm channel reflectances in order to constrain the retrieval algorithm, which will be discussed in the next section.

3.2 Retrieval Algorithm

A new cloud retrieval algorithm has been in development that exploits the synergy of MODIS and CloudSat measurements. Our baseline assumption is that any detected liquid phase cloudy volume is potentially composed of two modes of hydrometeors – clouds (small hydrometeors) and precipitation (large hydrometeors). Since accurate retrievals depend on a correct particle size distribution (PSD) shape (Mace 2010), we assume a bimodal PSD in our retrieval to simultaneously characterize the cloud and precipitation modes.

The satellite measurements contain independent but tangled information about the cloud and precipitation hydrometeors that may coexist within a cloudy profile. For example, the CloudSat CPR is most sensitive to the largest hydrometeors because the radar reflectivity is dependent on the sixth power of the particle size. Therefore, when precipitation is present, CloudSat will respond primarily to the precipitation sized

hydrometeors. Otherwise, in the absence of precipitation, the radar will interact primarily with the cloud droplets that characterize the cloud mode. Additionally, the MODIS visible reflectance is sensitive to and provides information primarily about cloud properties, while the MODIS near-infrared reflectance supplies some information about precipitation properties. Further still, a new measurement developed by Simone Tanelli from NASA Jet Propulsion Laboratory gives 94 GHz brightness temperature derived from CloudSat's CPR noise variations (see West 2014 for a detailed description of this product). Analogous to a passive microwave measurement, which responds to a cloud's water path, the brightness temperature is primarily sensitive to the cloud mode when cloud water dominates precipitation water, but provides a small contribution from the precipitation mode when precipitation is present. It is well known that microwave radiometry is a critical passive constraint for retrievals of liquid cloud properties (Frisch et al. 1998). In summary, this array of measurements allows us to simultaneously extract information for both cloud and precipitation sized hydrometeors.

The retrieval algorithm utilizes an optimal estimation framework (Rodgers 2000) to calculate an estimated state of the atmosphere that matches the actual state of the atmosphere as inferred from the mentioned measurements using a suite of forward models that link measurements and atmospheric state. Doing so allows us to depict and understand cloud properties as accurately as possible. However, by assuming that each volume within the column can have cloud and precipitation droplet modes, there are typically many degrees of freedom to the solution. With that in mind, distinctly different but physically reasonable atmospheric states can often be found that reproduce the measurements. Because the optimal estimation algorithm is not capable of choosing

among multiple solutions, it is critical that the initial or first guess state be reasonably

close to what is considered to be the most physically reasonable and nearly final solution.

A first guess algorithm within the retrieval is responsible for generating a set of

PSD parameters used to ultimately calculate cloud properties in the optimal estimation

algorithm. We assume a modified gamma particle size distribution (a three-parameter

gamma distribution) given by

$$N(D) = \frac{N_x D^\alpha}{L_x^\alpha} \exp(-\frac{D}{L_x}) \tag{7}$$

where $N(D)$ has units of cm^{-3} cm^{-1} and represents the number of droplets per unit

volume per unit interval of droplet size. The parameters N_x (cm^{-3} cm^{-1}) and L_x (cm) are

often known as the intercept and slope, respectively, and α (unitless) is often referred to

as the shape parameter of the distribution (Petty and Huang 2011). It is these parameters

that are calculated within the first guess framework. The variable D has units of length,

as it represents the droplet size. Note that equation (7) is a general representation of the

PSD we use. For our bimodal assumption, we add the small mode and large mode

representations of equation (7) to get the combined mode PSD such that

$N(D) = N_s(D) + N_l(D)$.

In order to solve for N_x and L_x, we need an estimated liquid water content

(LWC) and cloud droplet number concentration. We start by using a method by Lebsock

et al. (2011), wherein we assume that two-thirds of the LWP fraction is due to cloud and

one-third due to precipitation. Next, we estimate a column-averaged modified gamma

PSD that is consistent with an estimated column visible optical depth and liquid water

path. Using the estimated PSD parameters from the column-averaged PSD and by taking

the first moment of the PSD, we calculate a column N_d, which is assumed to remain constant throughout the cloud layer (Miles et al. 2000). Then, using an approach by Frisch et al. (1998), we derive an initial estimate of the LWC profile, denoted as LWC_F. We then assume that the actual estimated LWC follows an adiabatic shape within the cloud layer, which we call LWC_E. Finally, we have an estimated N_d and LWC to calculate the parameters of the PSD.

Using the PSD parameters, we first calculate the cloud mode radar reflectivity Z_{est} and compare it to the measured CloudSat value Z_{obs} using a forward model described by Posselt and Mace (2014). Then, we redistribute our estimated LWC by taking water from LWC_E where $Z_{est} > Z_{obs}$ to where LWC_E is less than LWC_F until $Z_{est} \leq Z_{obs}$. Next, we take the remaining radar reflectivity values, if present, along with the one-third LWP fraction following Lebsock et al. (2011) and calculate a second modified gamma distribution indicative of the precipitation mode of the bimodal PSD. Following this procedure, we produce an estimated state to describe the cloud and precipitation properties.

Radiative transfer forward models link our estimated measurements to the actual measurements from the satellites. For instance, the resulting PSD parameters from the first guess algorithm are input into a radiative model to derive reflectances at the MODIS channels (Christi and Gabriel 2003), which operates on the single scattering properties of the hydrometeors using Mie theory (Bohren and Huffman 1998). These calculated reflectances based upon the first guess can then be compared to the measured reflectance values from MODIS. Similarly, a microwave model (Kummerow et al. 1996 with modification and improvements described by Lebsock et al. 2011) is used to calculate the

94 GHz brightness temperature, which can be compared to the measured CloudSat value. If the calculated values do not match the measured values to within a 10% fractional difference, then inputs (LWP and optical depth) to the first guess are adjusted. For example, if the calculated reflectance is higher than the measured reflectance, then the optical depth will be decreased by 10%. Once the fractional difference between our calculations and the observed measurements is less than or equal to 10%, or until the number of iterations reaches 10, the calculations that are closest to the measurements are stored and used.

An equivalent retrieval algorithm has also been developed to employ data from ARM instruments, which are ground based. We implemented this version of the retrieval using data from the MAGIC field campaign. Analogous measurements used to constrain this retrieval come from the following instruments. First, the Marine W-band (95 GHz) ARM Cloud Radar (MWACR) is a zenith pointing radar that provides radar reflectivity estimates. The MWACR is placed on a stabilizing table on the ship in order to ensure that the radar consistently remains vertically pointed, thus counteracting the rolling and pitching movements of the ship. In order to mitigate the effects of the ship's heave motion on the radar Doppler velocity measurements, we only use profiles in which the ship's heave velocity is zero. Second, the microwave radiometer (MWR), detects the microwave emissions of vapor and liquid water, providing brightness temperatures at 23.8 and 31.4 GHz. Third, the portable radiation package (PRP), provides shortwave broadband total downwelling irradiance.

3.3 Radiative Parameterization

An important component of the forward models used to compute the reflectances and shortwave fluxes is the calculation of the radiative properties of the cloud profile. There are three specific variables needed. They are the cloud optical depth τ, the asymmetry parameter g, and the single scatter albedo ω. Each of these variables will be described in the subsequent paragraphs, as well as the need for a radiative parameterization.

To begin, the basic interaction of radiation with clouds is determined by the wavelength of radiation and the size of the particle with which the radiation interacts (Stephens 1994, Bohren and Clothiaux 2006, Pretty 2006, Wallace and Hobbs 2006). This relationship, described as the particle size parameter, is defined as

$$x = \frac{\pi D}{\lambda} \tag{8}$$

where D is the diameter of a spherical particle, and λ is the wavelength of radiation. This is a useful metric as it helps to distinguish which radiative transfer theory to use (Petty 2006). For instance, given a particle size that is much smaller than the wavelength of radiation, Rayleigh theory will be used to describe radiative transfer in the atmosphere. In the case of sunlight interacting with cloud droplets, Mie scattering theory is used. For more examples, see Figure 6, which displays various particle-to-wavelength relationships along with the respective theories used to describe their interactions (Petty 2006).

Cloud optical thickness is a measurement that describes the attenuation of radiation through a cloud layer. It is expressed as

$$\tau = \int_{z_{bot}}^{z_{top}} \beta_e(z)\,dz \tag{9}$$
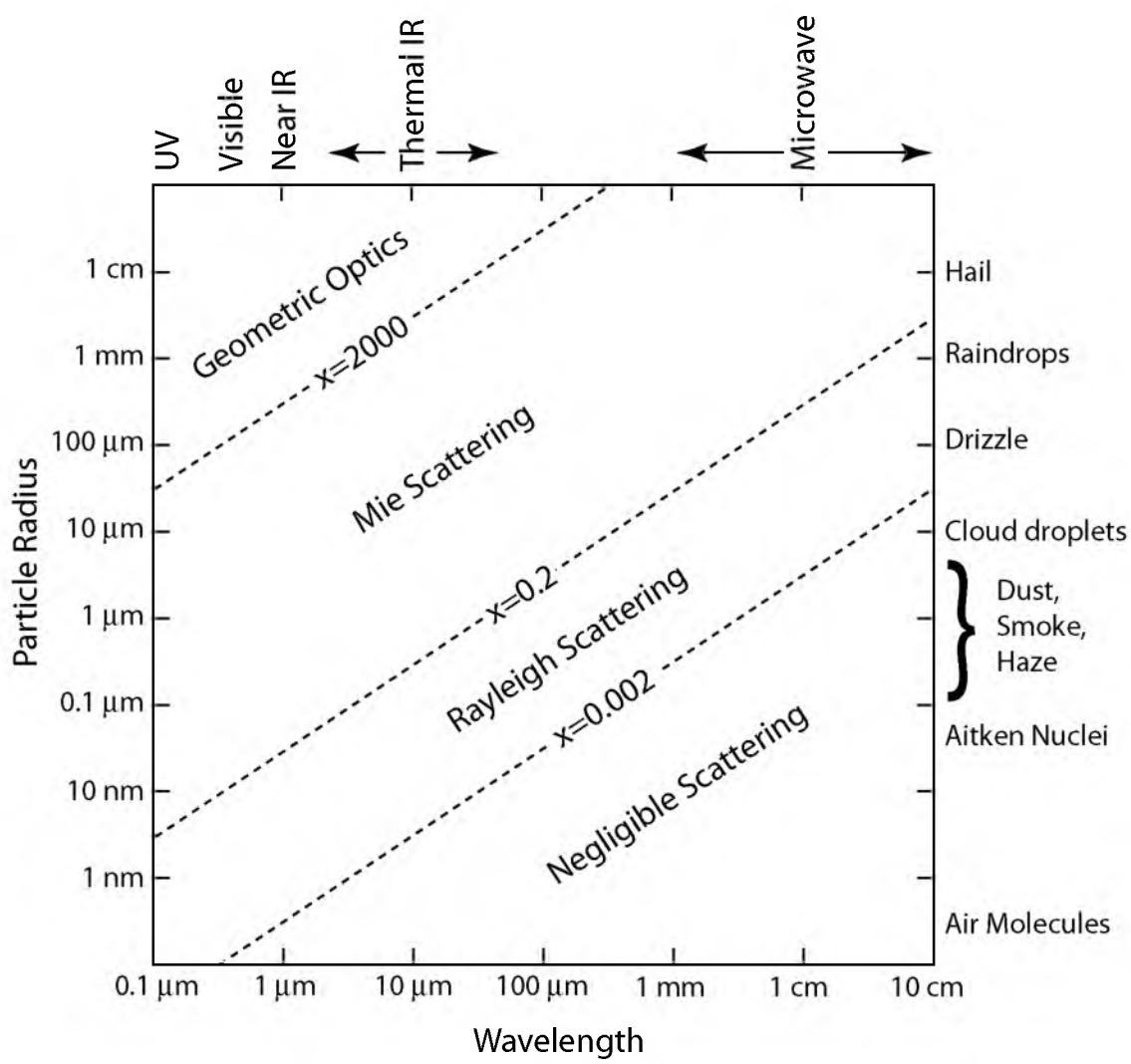
Figure 6. Relationship between particle size, radiation wavelength, and scattering behavior for atmospheric particles. Diagonal dashed lines represent rough boundaries between scattering regimes (reprinted from Petty 2006, © Grant W. Petty, used with permission).

where z_{top} is cloud top, z_{bot} is cloud base, β_e is the extinction coefficient, and dz is an increment of vertical depth (Petty 2006). The extinction coefficient represents the amount of radiation that is attenuated due to absorption, scattering, or both as it travels through the cloud. It can be calculated by taking the second moment of the PSD, shown here with the solution using equation (7) as the PSD

$$\beta_e = \int_0^\infty N(D)Q_e(D)\pi(\frac{D}{2})^2 dD = N_x L_x^3 \frac{\pi}{2}\Gamma(\alpha+3). \tag{10}$$

The extinction efficiency, Q_e, is the ratio of a particle's extinction cross-section (the area a single particle attenuates radiation) to its geometric cross-section (Petty 2006). The value of the extinction efficiency depends on the refractive index of the particle, the wavelength of radiation, and the size and shape of the particle (Stephens 1994). For spherical cloud droplets interacting with visible radiation (i.e., sunlight) $Q_e \approx 2$ (Petty 2006), which is an important assumption we make in our parameterization.

The single scatter albedo characterizes the relative importance of scattering and absorption of radiation through a cloud layer (Petty 2006, Wallace and Hobbs 2006). It is given by

$$\omega = \frac{\beta_s}{\beta_e} = \frac{\beta_s}{\beta_s + \beta_a} \tag{11}$$

where β_s is the scattering coefficient and β_a is the absorption coefficient (Petty 2006), both of which have similar definitions to the extinction coefficient. The single scatter albedo ranges from 0 to 1, where 0 indicates complete absorption of radiation and 1 indicates complete scattering of radiation. However, as Bohren (1987) states, these limits in the single scatter albedo are idealizations never realized in practice. In the case of cloud

droplets interacting with sunlight, we can ignore absorption and set the single scatter albedo to unity without making great errors (Bohren 1987). Implicit in the single scatter albedo for clouds is the refractive index of water. The imaginary component of the refractive index indicates the degree to which clouds absorb radiation and is dependent on the wavelength of radiation. At near-IR and IR wavelengths, liquid water is more absorbing, implying an increase in the imaginary component of the refractive index, which will ultimately result in a single scatter albedo less than unity because more radiation is being absorbed by the cloud water droplets. Refractive index values used in this study with their accompanying references are shown in Table 1.

The asymmetry parameter gauges the direction of scattered radiation. It ranges from -1 indicating complete back-scattered radiation to 1 for complete forward scattered radiation. We calculate the asymmetry parameter using the following equation

$$g = \frac{1}{\beta_s} \int_0^\infty N(D) Q_s(D) \pi (\frac{D}{2})^2 g(D) dD \qquad (12)$$

where Q_s is the scattering coefficient and $g(D)$ gives the average $\cos\theta$ scattering direction for a large number of scatter photons (Petty 2006). For solar wavelengths and cloud droplets, the asymmetry parameter is quasi-constant with an approximate value of 0.85 (Stephens 1994), which implies that cloud droplets are strongly forward scattering. Physically, this means a photon interacting with a cloud droplet is more likely to be scattered into a direction that is not too different from its previous direction of travel, more likely reaching the cloud base than leaving at cloud top (Petty 2006).

Mie scattering theory is used to calculate the radiative parameters above for cloud droplets at the 0.55 μm and 2.1 μm MODIS reflectance channels (see Figure 6 for the scattering regime at these wavelengths for cloud droplets). Plots of the extinction

Table 1. Refractive indices of water used in the calculation of the single scattering properties of the cloud droplets for the single wavelengths 0.55 and 2.1 μm. Note, in order to avoid the potential peaks in energy described by Mie theory, it is better to consider a wavelength bandwidth to calculate the radiative properties of cloud droplets.

Wavelength (μm)	Refractive Index	Reference
0.55	$1.333 + i1.96e - 9$	Hale and Querry (1973)
2.1	$1.291 + i4.403e - 4$	Segelstein (1981)

efficiency, co-albedo $(1-\omega)$, and asymmetry parameter as calculated by Mie theory at the 0.55 μm and 2.1 μm wavelengths are shown in Figure 7 and Figure 8, respectively, as a function of the particle size parameter. Immediately noticeable is the difference in the co-abledo between the wavelengths for size parameters in excess of about 50. As mentioned earlier, this is due to the fact that liquid water is more absorbing of radiation at near-IR wavelengths such as the 2.1 μm channel. On the other hand, the extinction efficiency and asymmetry parameter exhibit little change between the two wavelengths.

Since Mie scattering is computationally expensive to calculate, it is necessary and convenient to produce a parameterization (Slingo 1989). Parameterizations for the shortwave radiative properties of clouds have long been developed and implemented (Slingo 1989, Hu and Stamnes 1993). However, most of these parameterizations assume a single mode particle size distribution and are valid for only a small range of cloud droplet sizes and spectral ranges.

Because we assume a bimodal PSD in our retrieval algorithm, we need to create a new radiative parameterization to account for that. As Slingo (1989) demonstrated, the radiative properties of water clouds can be parameterized as a function of liquid water path and effective radius. The effective radius is defined by taking the third moment of the PSD to the second moment as follows

$$r_e = \frac{\int_0^\infty N(D)(\frac{D}{2})^3\, dD}{\int_0^\infty N(D)(\frac{D}{2})^2\, dD} = \frac{L_x \Gamma(\alpha+4)}{2\Gamma(\alpha+3)}. \tag{13}$$

The effective radius is a cross-sectional area-weighted mean size, which makes it applicable for radiative applications. With that in mind, Slingo (1989) developed linear
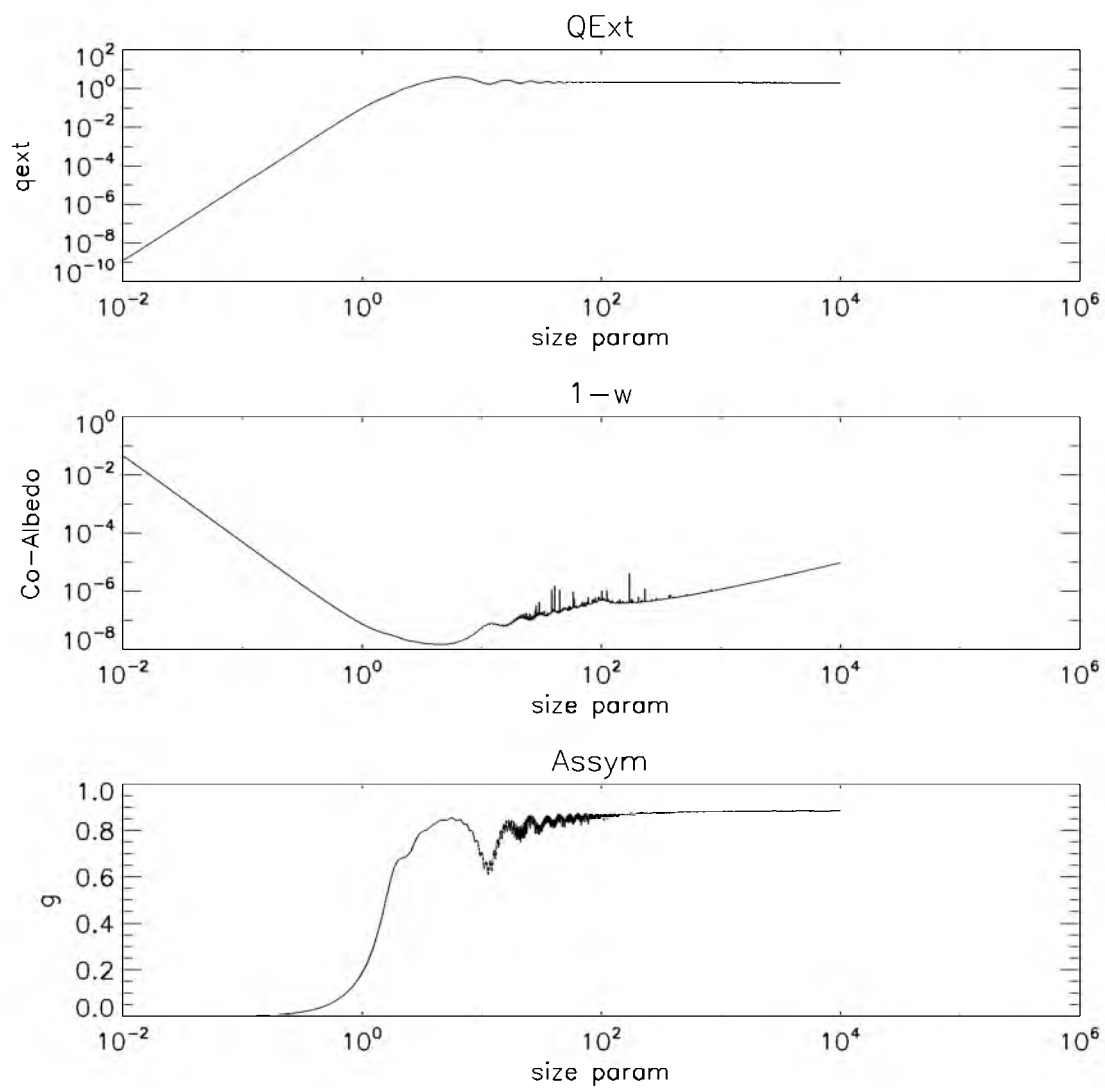
Figure 7. The extinction efficiency (top), co-albedo (middle), and asymmetry parameter (bottom) plotted as a function of the particle size parameter at the 0.55 μm wavelength.
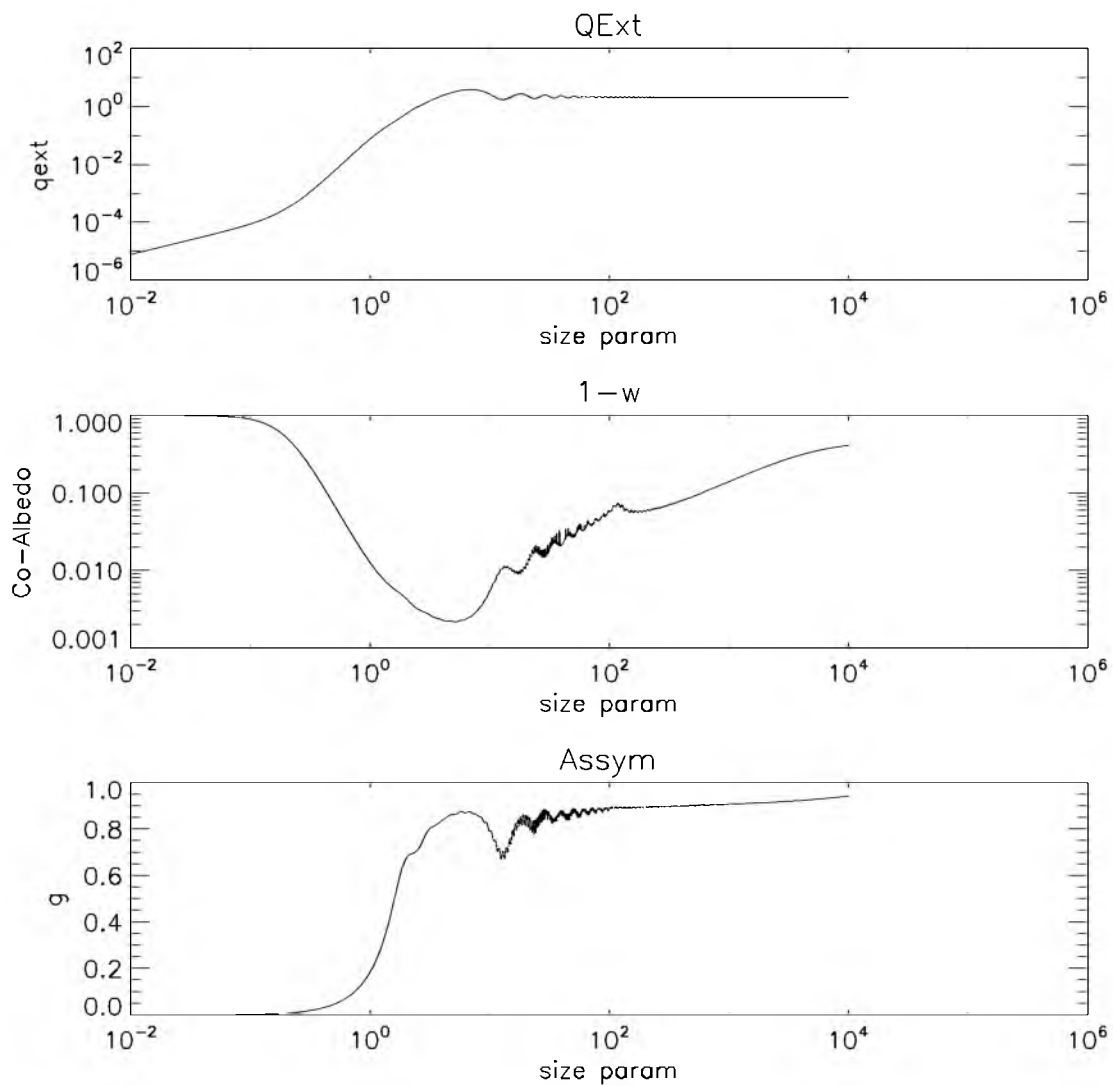
Figure 8. Same as in Figure 7 except at the 2.1 μm wavelength.

parameterizations for τ, ϖ, and g for a narrow effective radius range from 4.2 to 16.6 μm and at a spectral range from 0.25 to 4.0 μm. Though these parameterizations are for single mode distributions, they serve as a validation tool to compare against the small mode parameterization we develop.

Hu and Stamnes (1993), on the other hand, point out that for larger drop radius sizes (> 12 μm), a linear parameterization will no longer be successful for the single scatter albedo and asymmetry parameter. For this reason, they use a nonlinear least-square regression for their parameterizations. For our radiative parameterization, we use a linear regression for the extinction coefficient after Slingo (1989) and a nonlinear regression for the single scatter albedo and asymmetry parameter following Hu and Stamnes (1993).

The basis for the parameterization we have developed is as follows. First, we make a parameterization for τ, ω, and g for each size mode, one for the cloud mode and one for precipitation. Second, we combine the two parameterizations to create a single parameterization to simultaneously represent the radiative properties of both modes as a combined effect. Because of the linear nature of the extinction coefficient, the small mode and large mode parameterizations can simply be added to form the combined mode parameterization. However, for the asymmetry parameter and the single scatter albedo, we weight the small and large mode parameterizations with their respective extinction coefficients and then add the two parameterizations for the combined mode. The mathematical representation of the parameterizations is shown in Table 2.

In order to create the parameterizations, it is first necessary to make the calculations of τ, ω, and g at the wavelength channels mentioned earlier. This is done

Table 2. Mathematical representation of the small (cloud), large (precipitation), and combined mode (both) of the radiative parameterizations. Note, the subscripts s, l, and b refer to the respective modes.

Small Mode	Large Mode	Combined Mode
$\beta_{e,s} = lwc_s(a_s + \dfrac{b_s}{r_{e,s}}) + const_s$	$\beta_{e,l} = lwc_l(a_l + \dfrac{b_l}{r_{e,l}}) + const_l$	$\beta_{e,b} = \beta_{e,s} + \beta_{e,l}$
$g_s = g_{so}r_{e,s}{}^{g_{s1}} + g_{s2}$	$g_l = g_{lo}r_{e,l}{}^{g_{l1}} + g_{l2}$	$g_b = \dfrac{\beta_{e,s}}{\beta_{e,b}}g_s + \dfrac{\beta_{e,l}}{\beta_{e,b}}g_l$
$\omega_s = 1 - (\omega_{so}r_{e,s}^{\omega_{s1}} + \omega_{s2})$	$\omega_l = 1 - (\omega_{lo}r_{e,l}^{\omega_{l1}} + \omega_{l2})$	$\omega_b = \dfrac{\beta_{e,s}}{\beta_{e,b}}\omega_s + \dfrac{\beta_{e,l}}{\beta_{e,b}}\omega_l$

using the bhmie code developed by Bohren and Huffman (1998), which uses Mie

scattering theory to compute $Q_e(D), Q_s(D),$ and $g(D)$ inherent in equations (10), (11), and

(12). The same equations are then numerically integrated with an IDL routine that

utilizes a modified Romberg quadrature method.

This process is done for each individual mode as well as for the combined mode.

The results are then used to create the radiative parameterizations as a function of radius

and LWC. The linear regression for the extinction coefficient was performed in IDL

using the regress function, which implements a multiple linear regression fit. The

nonlinear regression for the single scatter albedo and asymmetry parameter was

performed using IDL's comfit function, which utilizes a gradient-expansion least-squares

method to return a nonlinear fit of the form $y = a_o x^{a_1} + a_2$. At the 0.55 μm wavelength,

the absorption of radiation by a cloud droplet is negligible, and so scattering is the

dominant process (Slingo 1989, Petty 2006). Therefore, the single scatter albedo at this

wavelength is set to unity. Table 3 lists the coefficients for the resulting

parameterizations. Note, all units are in cgs.

Scatter plots comparing our parameterization (y-axis) vs. the calculated values

from the bhmie code (x-axis) are shown in Figures 9 and 10. As expected, the extinction

does not vary much between the two different wavelengths. This is because the

extinction coefficient is only weakly dependent on the wavelength within the calculated

spectral band (Slingo and Schrecker 1982). The co-albedo (coa) is shown in the plots

instead of the single scatter albedo. At wavelengths shorter than 1 μm, absorption is

negligible, whereas beyond this wavelength, there are distinct absorption bands correlated

to the bands of water vapor (Slingo and Schrecker 1982). Thus only the near-IR bands

Table 3. Values of the coefficients from Table 2 of the radiative parameterizations for the small and large modes at the MODIS channel wavelengths. Note that the optical depth is obtained by multiplying extinction by the cloud thickness as shown in equation (9)

Extinction Parameterization		
Channel Wavelength (μm)	Small Mode	Large Mode
0.55	$a_s = -8.903e-6$ $b_s = 1.500$ $const_s = 1.714e-12$	$a_l = 5.575e-6$ $b_l = 1.500$ $const_l = 8.579-10$
2.1	$a_s = -9.005e-6$ $b_s = 1.500$ $const_s = 1.559e-12$	$a_l = 5.571e-6$ $b_l = 1.500$ $const_l = 8.595e-10$
Asymmetry Parameter Parameterization		
0.55	$g_{so} = 0.769$ $g_{s1} = 0.035$ $g_{s2} = 0.256$	$g_{lo} = 0.471$ $g_{l1} = 0.022$ $g_{l2} = 0.461$
2.1	$g_{so} = 0.858$ $g_{s1} = 0.099$ $g_{s2} = 0.406$	$g_{lo} = 1.13$ $g_{l1} = 0.030$ $g_{l2} = -0.070$
Single Scatter Albedo Parameterization		
0.55	$\omega_{s0} = 0$ $\omega_{s1} = 0$ $\omega_{s2} = 0$	$\omega_{l0} = 0$ $\omega_{l1} = 0$ $\omega_{l2} = 0$
2.1	$\omega_{s0} = 1.072$ $\omega_{s1} = 0.438$ $\omega_{s2} = -0.027$	$\omega_{l0} = 0.889$ $\omega_{l1} = 0.043$ $\omega_{l2} = -0.637$
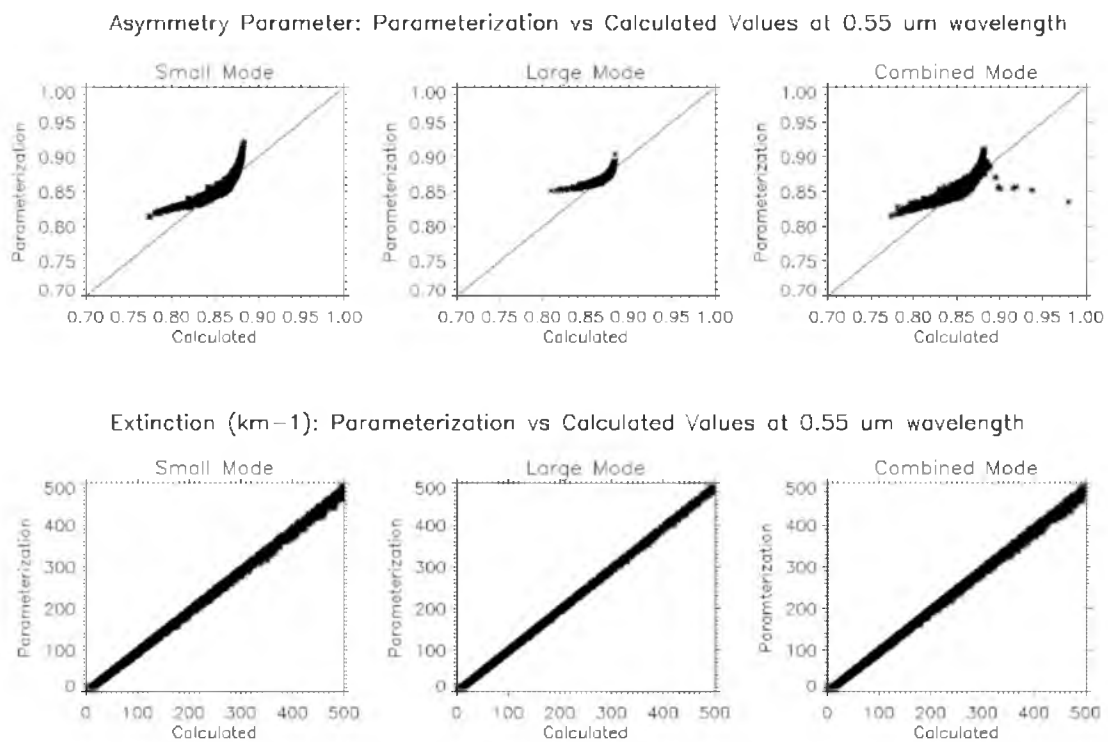
Figure 9. Scatter plots comparing our new parameterization at each mode to the calculated values for the asymmetry parameter (top) and extinction (bottom) at the 0.55 μm wavelength.
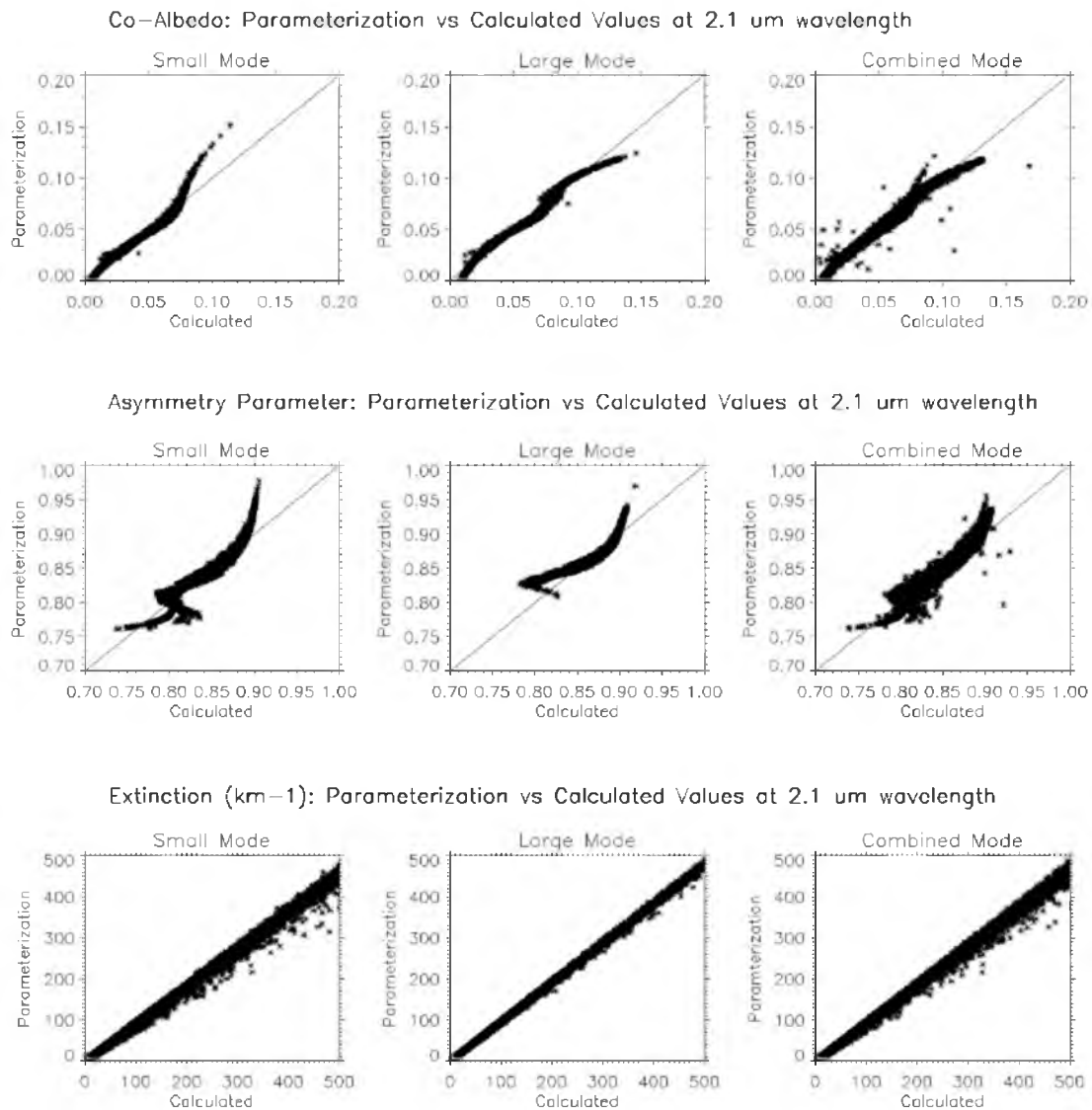
Figure 10. Same as in Figure 9 except for the 2.1 μm wavelength.

for the co-albedo are shown in the mentioned figures. Note the nonlinear nature of the co-albedo as well as the asymmetry parameter.

Comparisons of our small mode parameterization to Slingo's parameterization are shown in Figures 11 and 12. In order to make this comparison, it was necessary to use only the effective radius range for which Slingo's parameterization is valid. Notice that the optical depth matches well at each wavelength. This is because the optical depth is well represented by a linear parameterization. On the other hand, there are noticeable differences in the plots comparing the single scatter albedo and asymmetry parameter. Perhaps the reason for this is due to the fact that our parameterization is nonlinear and Slingo's parameterization is linear.
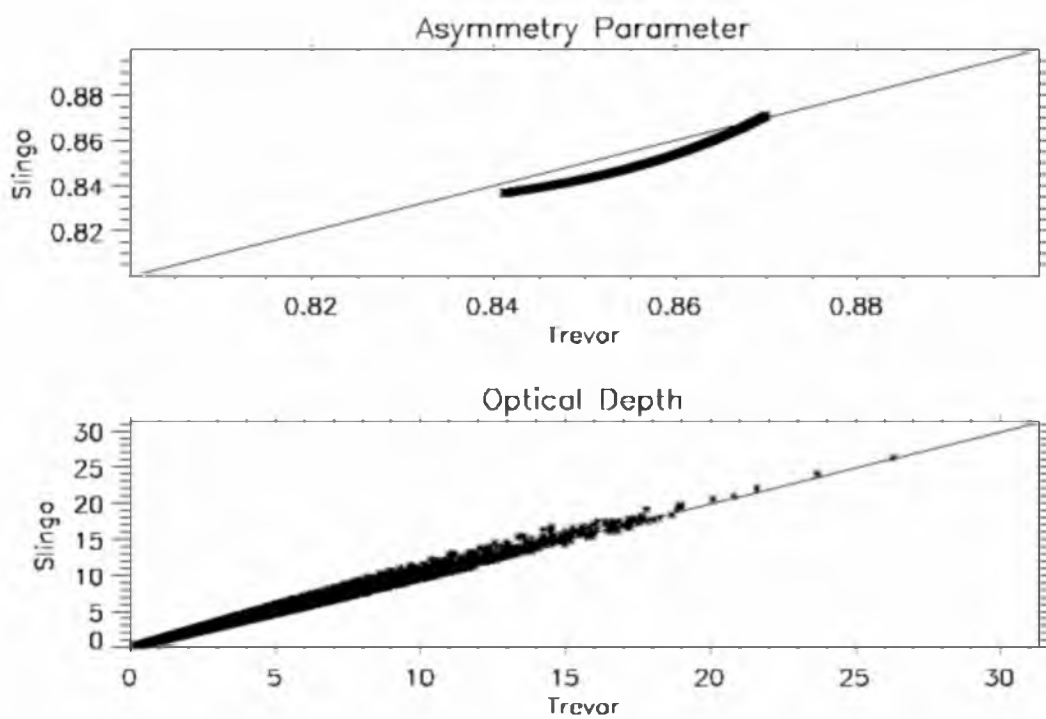
Figure 11. Scatter plot comparing our small mode parameterization to Slingo's parameterization at the 0.55 μm wavelength.
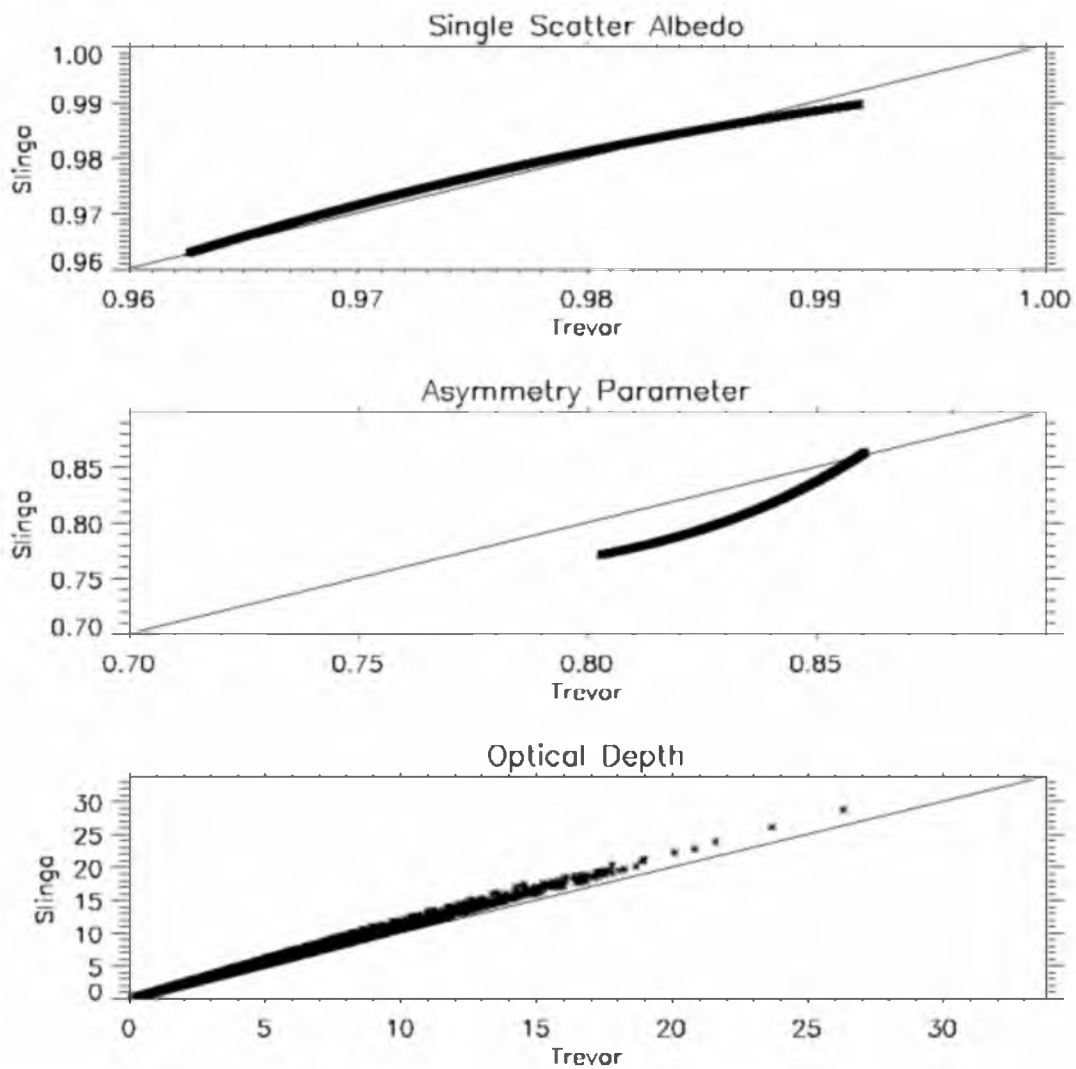
Figure 12. Same as in Figure 11 except for the 2.1 μm wavelength.

CHAPTER 4

RESULTS

4.1 MAGIC Transect Region Using A-Train Data

Once the PSD parameters have been generated, cloud albedo can be determined

by using a two-stream approximation based upon Bohren (1987)

$$A = \frac{(1-g)\tau}{1+(1-g)\tau}.$$ (14)

According to Bohren, this equation is reasonable for diffuse radiation such as that

scattered by clouds. However, for a direct source of radiation, there is a factor of $\sqrt{3}$ that

should be included in the equation as explained by Meador and Weaver (1980). For our

research, we used equation (14) since previous studies of albedo susceptibility (i.e.,

Platnick and Twomey 1994, Painemal and Minnis 2012) reference the same equation.

We calculate the albedo values at the 0.55 μm wavelength. The variables τ and g are

calculated based upon the radiative parameterization as explained in the previous section.

The calculated albedo, precipitation rates, and cloud droplet number

concentrations were binned at every 40 g m^{-2} from 0 to 400 g m^{-2} LWP. Figure 13 shows

the linear regressions of A to $\ln N_d$ at each LWP bin for the MAGIC region using A-Train

data during June, July, and August (JJA) for the year 2008. Recall that the slope of the

linear regression represents the albedo susceptibility, which is shown in Figure 14 using

the results from Figure 13. Error bars for the susceptibilities are obtained by taking the 1-
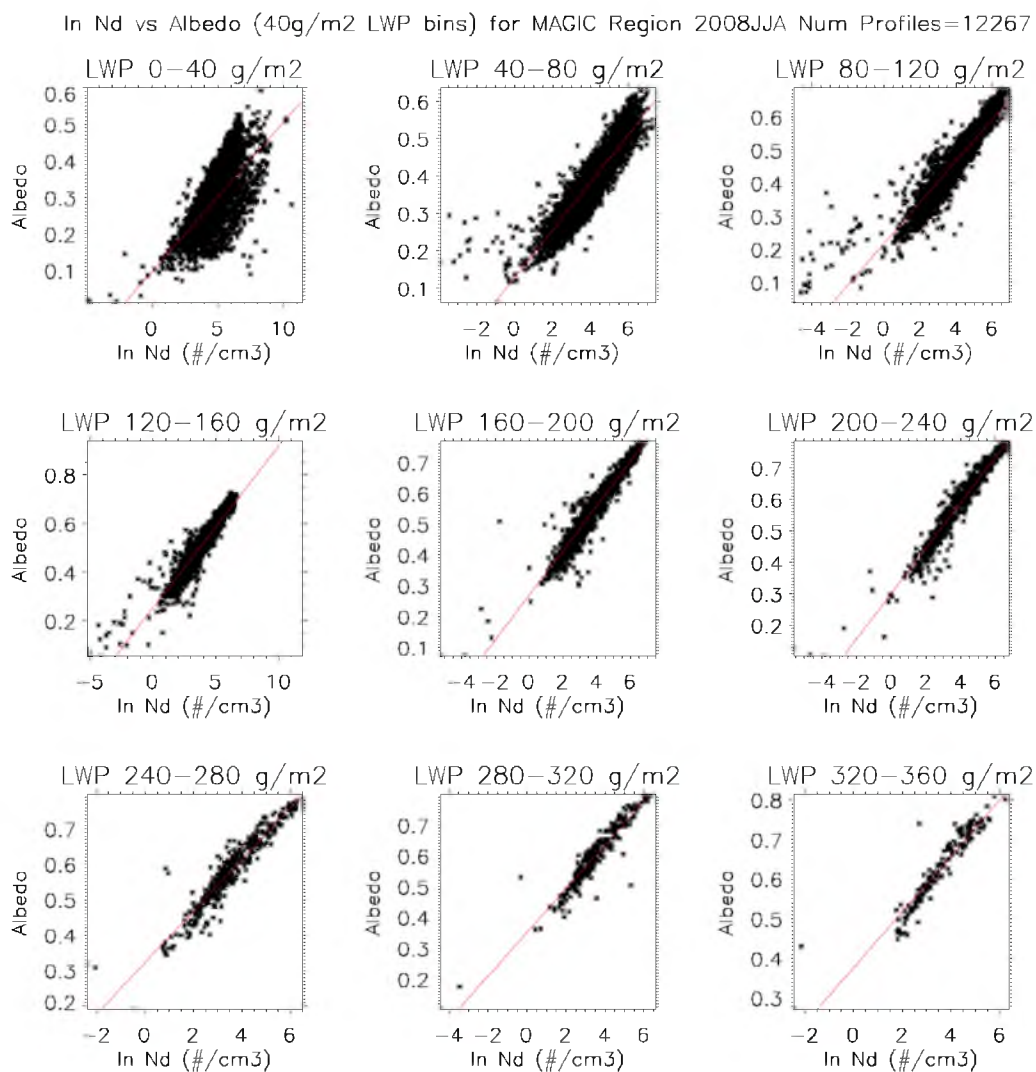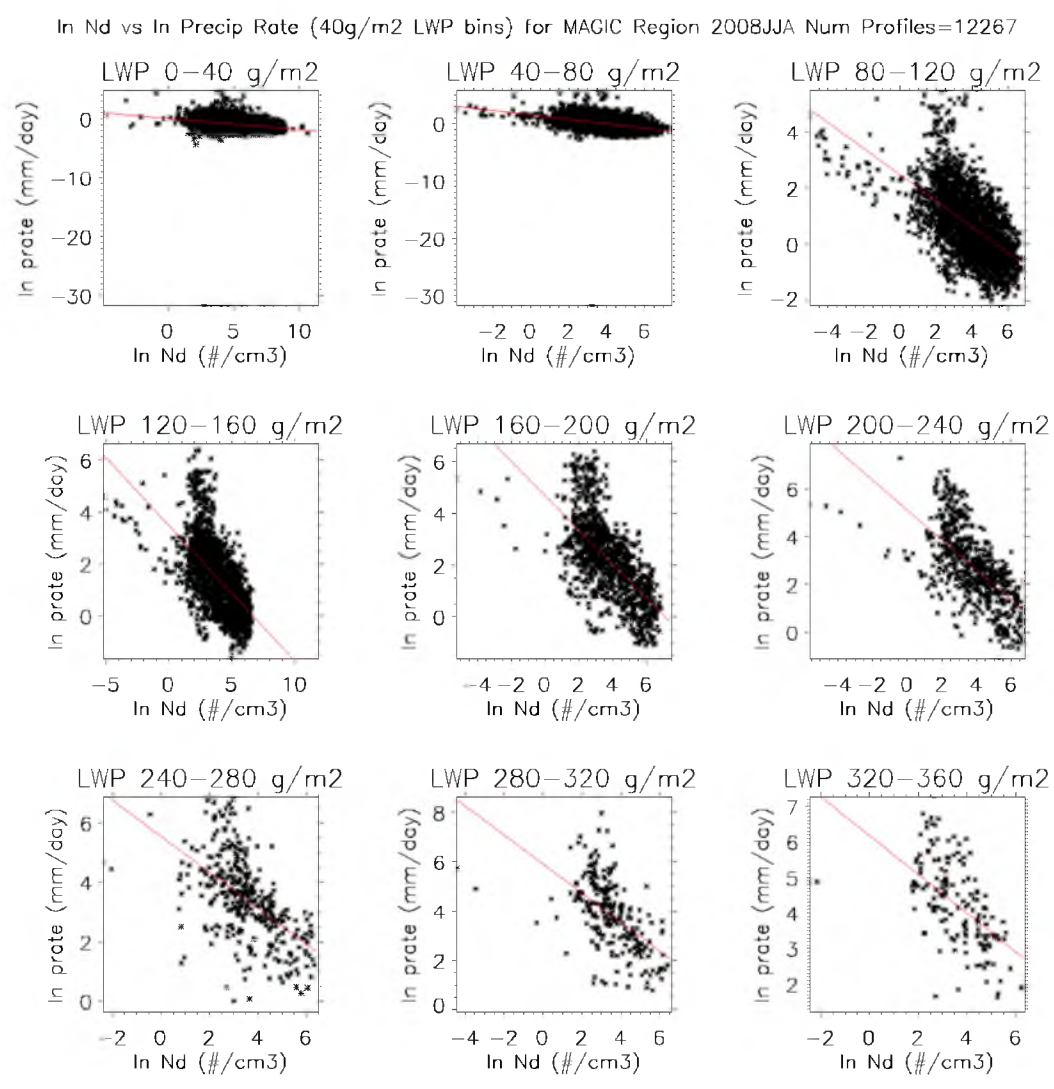
Figure 13. Linear regression of A to $\ln N_d$ at 40 g m^{-2} LWP bins for the MAGIC region on JJA 2008 using A-Train data.
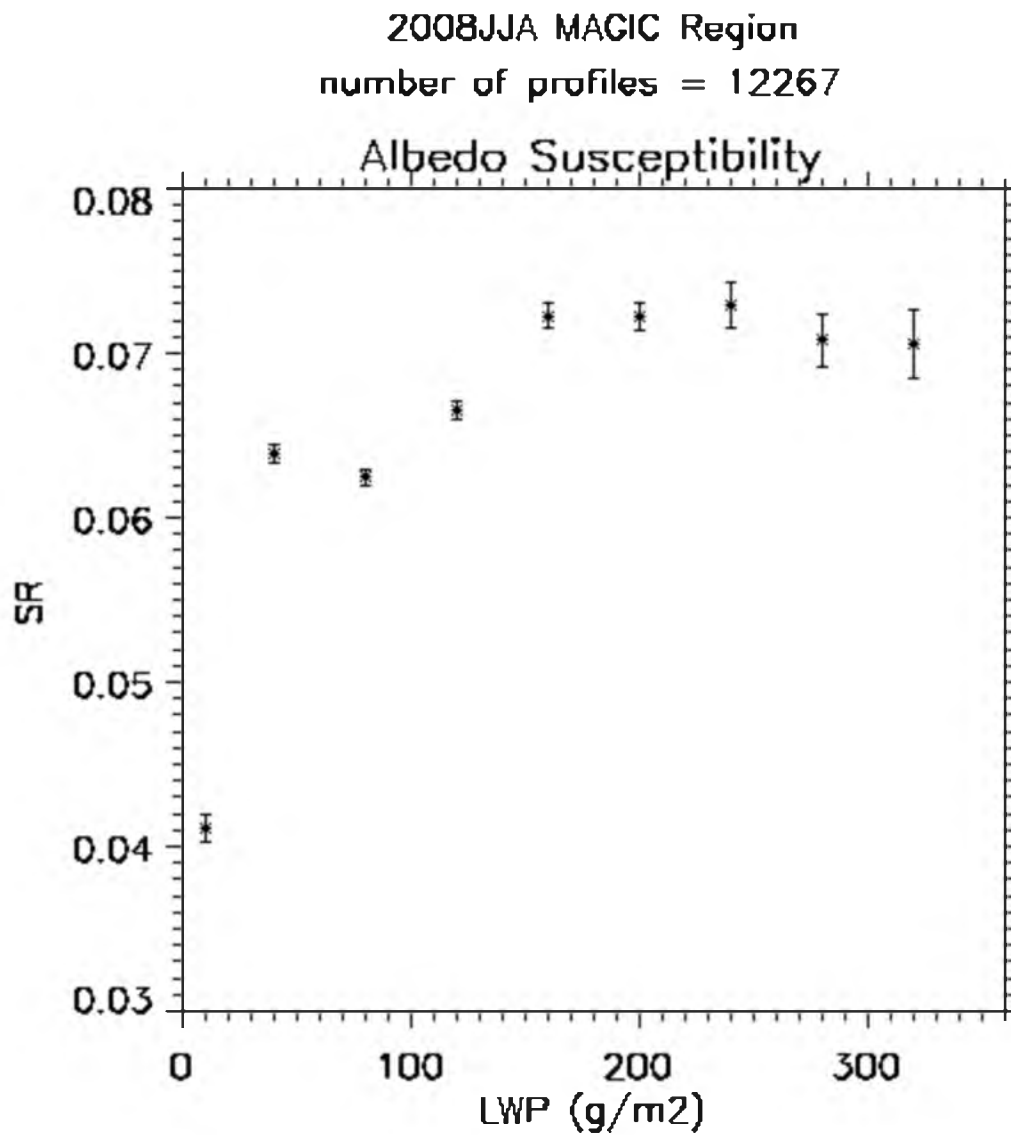
Figure 14. The resulting albedo susceptibility plot from Figure 13. Each data point represents the slope from the linear regression of A to $\ln N_d$ at the respective LWP bins.

sigma uncertainty estimates of the slopes of the linear regression, which is determined using the linfit function in IDL. Notice from Figure 14 that the lowest LWP bin exhibits the lowest susceptibility, and that as LWP increases to 360 g m^{-2}, the susceptibility values level off. The study from Painemal and Minnis (2012) shows similar behavior for the albedo susceptibility of clouds near the coast, which are regions characterized by higher aerosol concentrations (see Figure 4). According to equation (14), the albedo susceptibility peaks at an optical depth around 13.33 for a constant asymmetry parameter 0.85, with a corresponding LWP path that depends on the cloud droplet effective radius (Painemal and Minnis 2012). This suggests that an inflection point has been reached with the cloud optical depth and the susceptibility remains constant or slightly decreases beyond this point.

Similarly, Figures 15 and 16 show the linear regressions at each LWP bin for the precipitation rate in the MAGIC region during JJA 2008 and the resulting precipitation susceptibility, respectively. Notice in Figure 16 that at low LWP (0-80 g m^{-2}), the slopes of the linear regression are small. Then, as the LWP increases, the precipitation susceptibility also increases until reaching a maximum and then decreases again. This pattern is similar to that produced by Sorooshian et al. (2009), wherein they suggested three different precipitation susceptibility regimes.

The next plots are unique. They show the correlation between the albedo and precipitation susceptibilities between two different seasons. Figure 17 displays the susceptibilities for the winter months (JFM), and Figure 18 for the summer months (JJA). What is immediately noticeable in the two figures is the difference in the precipitation susceptibility between the two seasons. There is an obvious inflection point in the

Figure 15. Linear regression of ln R (precipitation rate or prate) to ln N_d at 40 g m^{-2} LWP bins for the MAGIC region on JJA 2008 using A-Train data.
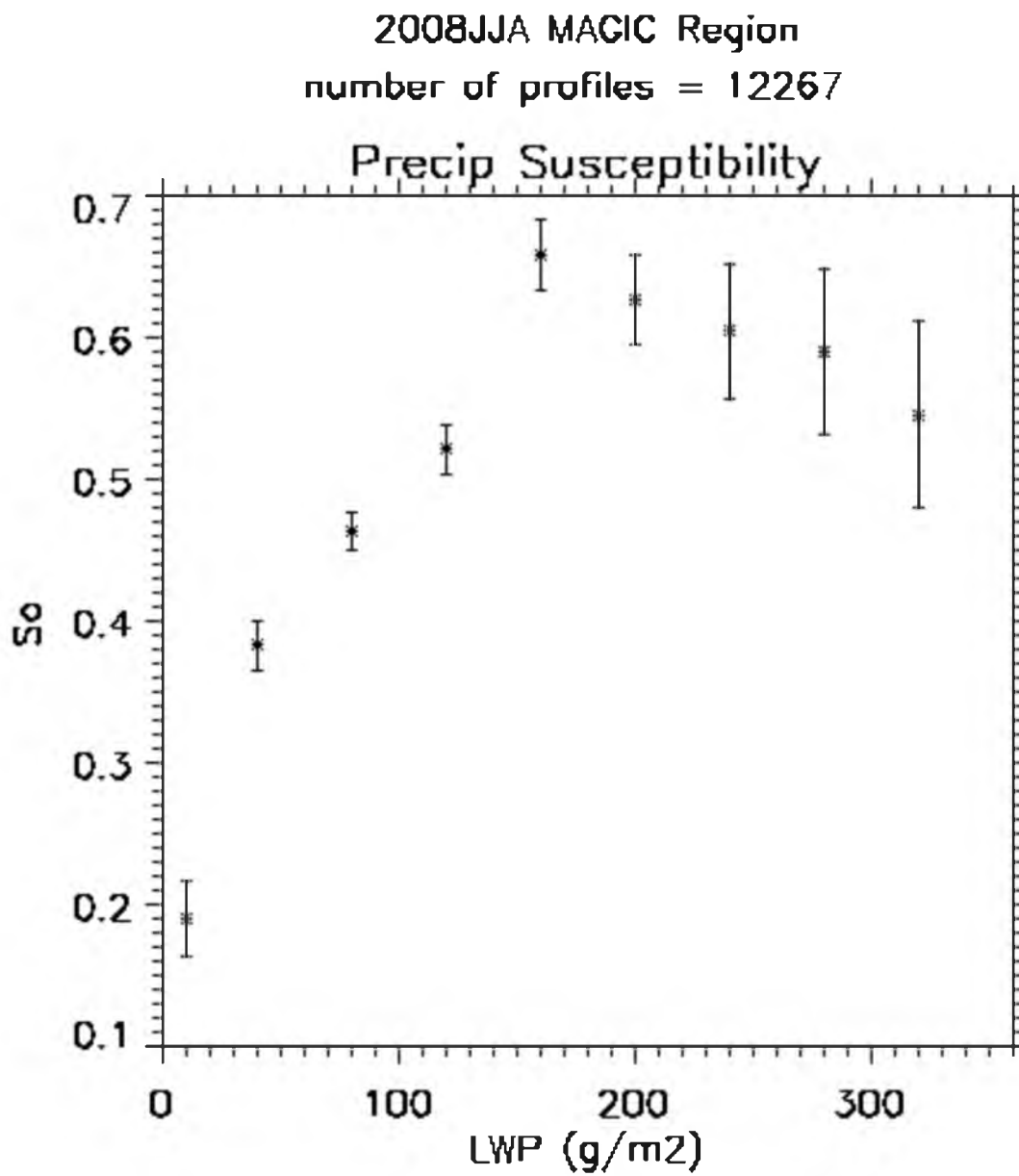
Figure 16. The resulting precipitation susceptibility plot from Figure 15. Each data point represents the slope from the linear regression of $\ln R$ to $\ln N_d$ at the respective LWP bins.
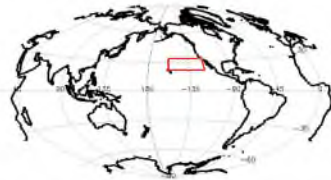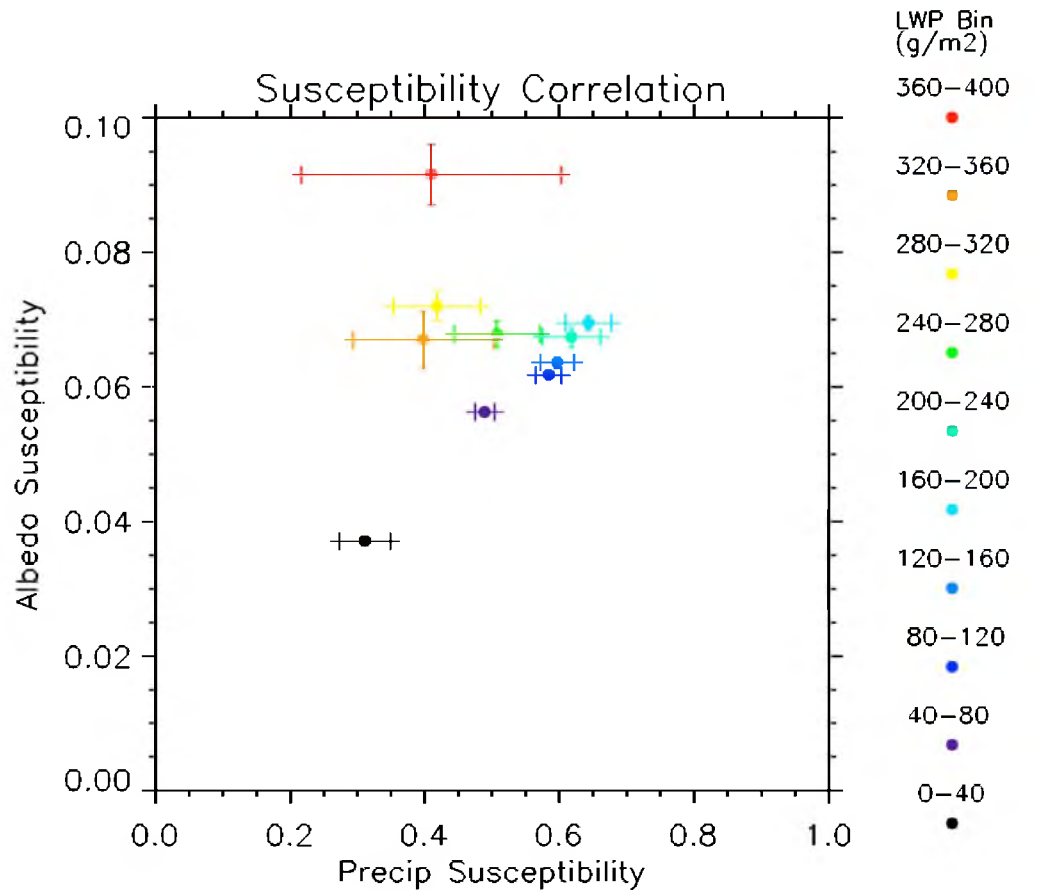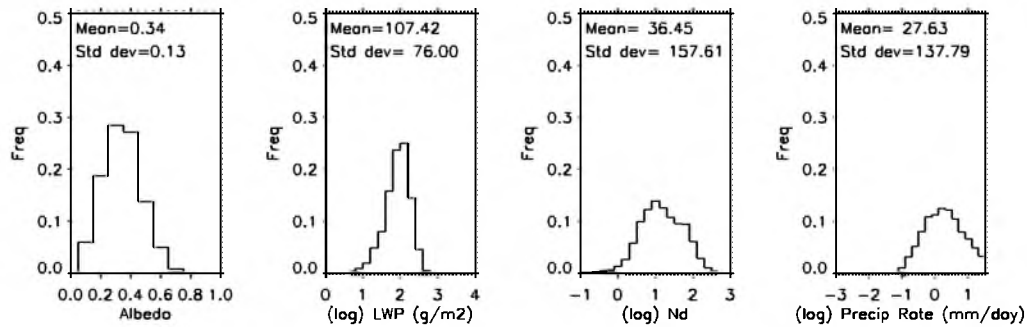
Figure 17. Relationship between albedo and precipitation susceptibility for the MAGIC region during JFM 2008 using A-Train data.
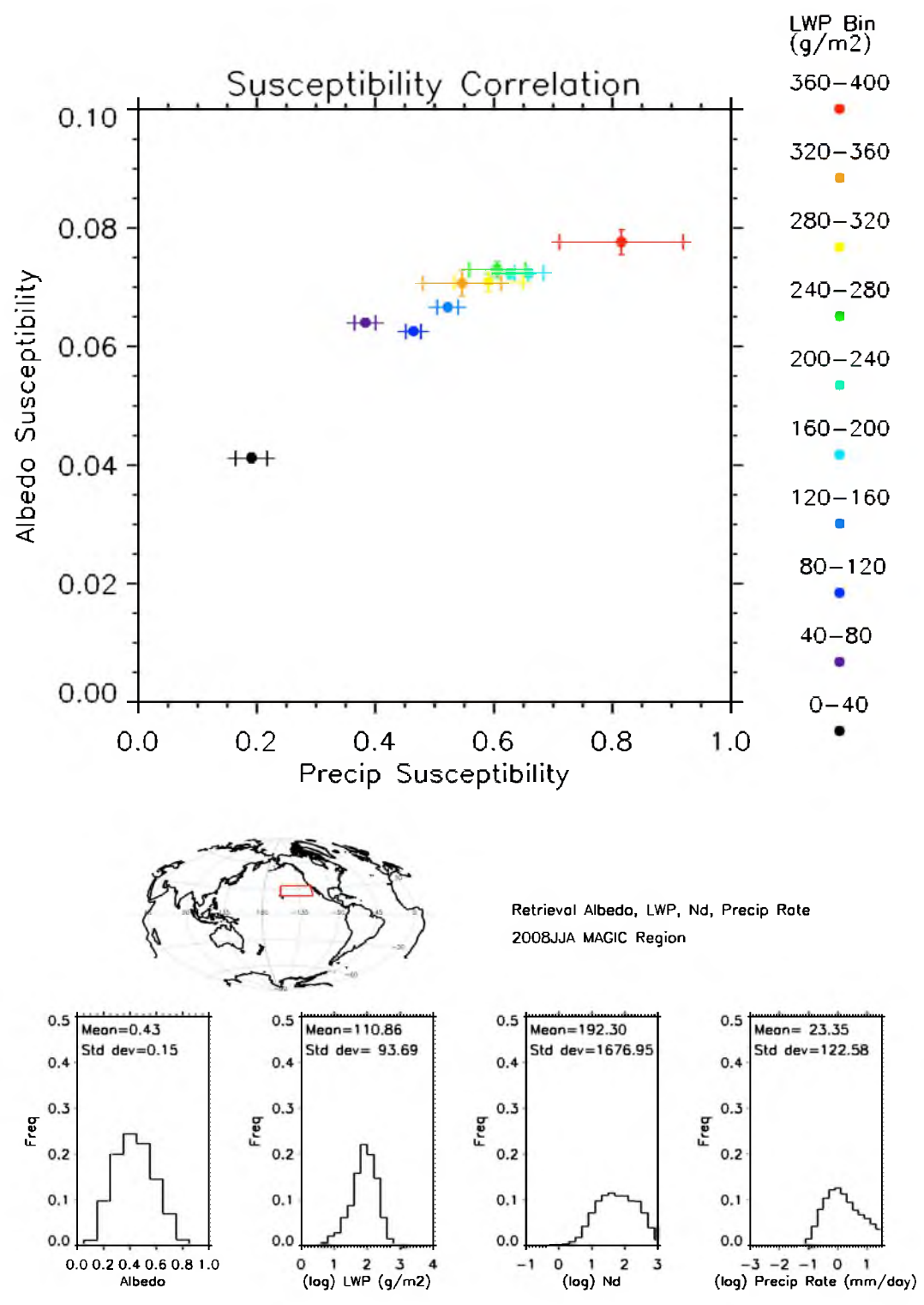
Figure 18. Same as in Figure 17 except for JJA 2008.

precipitation susceptibility in winter. The histograms show that in the winter, the mean cloud droplet number concentration is about 35 cm^{-3}, whereas for the summer months, the mean is much higher at roughly 190 cm^{-3}. It was mentioned earlier that clouds with higher cloud droplet number concentrations are more susceptible to precipitation suppression (2nd aerosol indirect effect). Therefore, it may be that in the winter months, the precipitation processes are more efficient due to the lower cloud droplet number concentration. This may explain why we see the inflection point in the precipitation susceptibility in the winter as the precipitation changes from an autoconversion regime at low LWP to an accretion regime at high LWP (Feingold et al. 2013). For the summer months, the higher droplet concentration may have suppressed the precipitation process such that the autoconversion regime is predominant. The albedo susceptibility, on the other hand, tends to exhibit more of a monotonic behavior, and does not change much between seasons.

Another approach to investigate the possible controls on the cloud albedo and precipitation susceptibility is to explore large-scale meteorological effects that may influence marine boundary layer cloud properties such as cloud droplet number concentration. To do this, we use the surface wind speeds provided by the ECMWF CloudSat data product, and separate the wind speeds into terciles. We plot the susceptibilities for all of the data points in the low surface wind speed tercile and compare the results to the susceptibilities in the high wind speed tercile, as shown in Figure 19 for the winter months and in Figure 20 for the summer months. Both seasons show large droplet concentrations in the high wind tercile, most noticeable in the summer months. This suggests a possible control of the surface winds on the aerosol
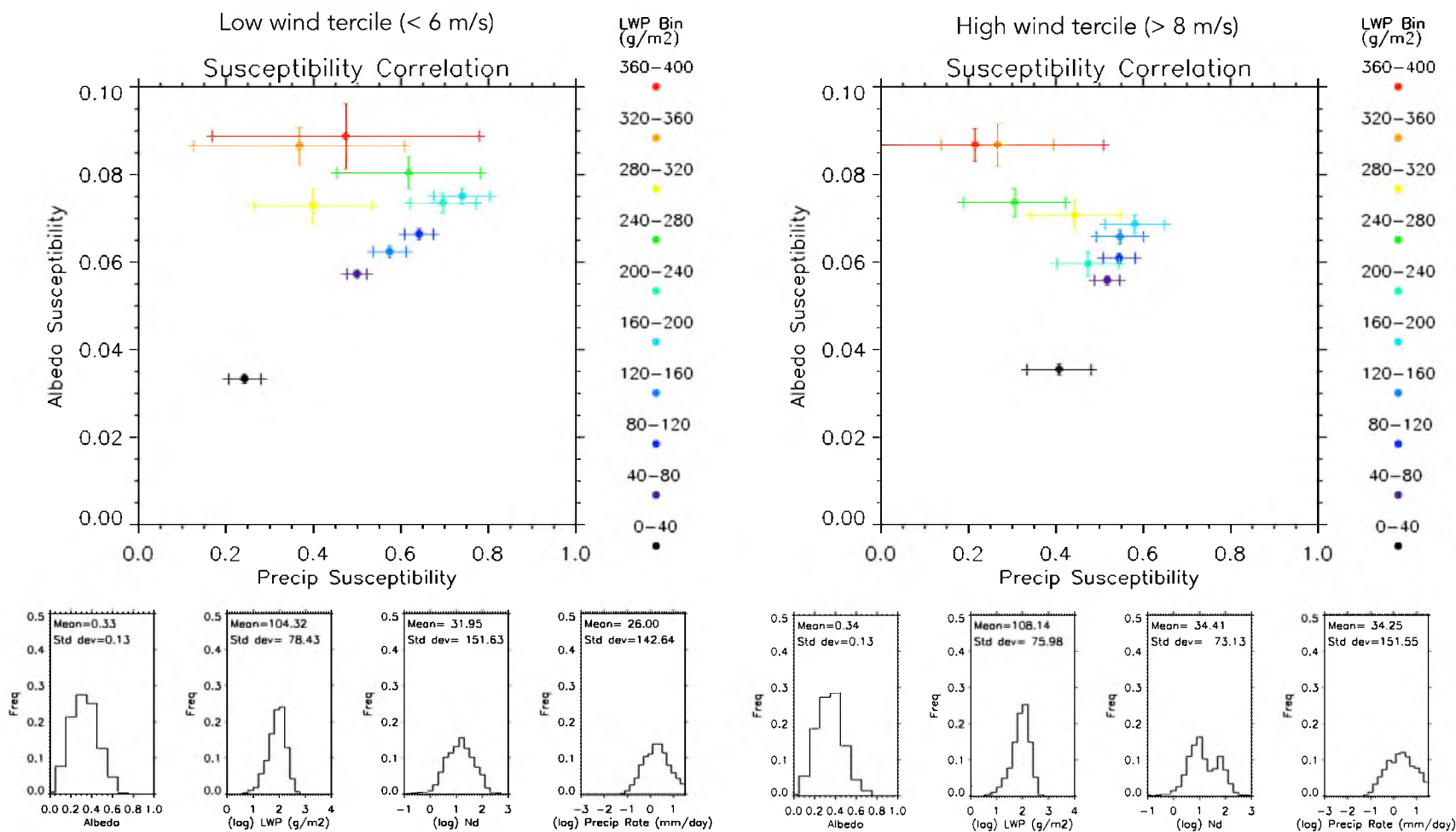
Figure 19. Susceptibility correlation divided into low surface wind conditions (left) and high surface wind conditions (right) for the MAGIC region during JFM 2008 using A-Train data.
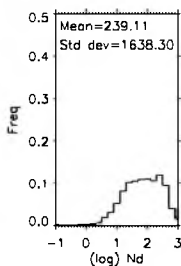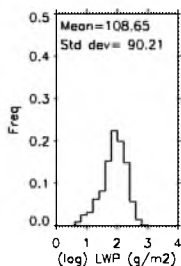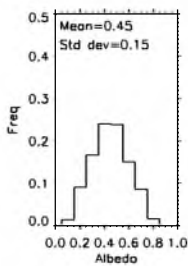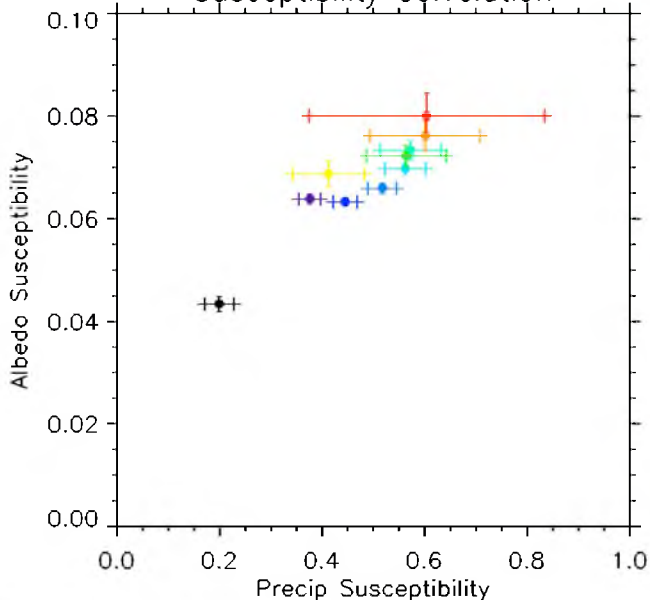
Figure 20. Same as in Figure 19 except for JJA 2008.

2008JJA MAGIC Region Number of Profiles = 4090

High wind tercile (> 7 m/s)

Susceptibility Correlation

LWP Bin (g/m2)
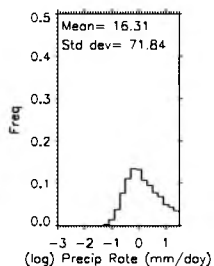
concentration that act as CCN (O'Dowd et al. 1997).

The albedo susceptibility shows little sensitivity within the two wind terciles shown. However, during the winter months when the droplet concentration is smaller, the albedo susceptibility increases with increasing LWP. On the other hand, during the summer months when the droplet concentration is higher, the albedo seems to level off with increasing LWP. Additionally, the winter months exhibit a higher susceptibility at larger LWP values than do the summer months. Figure 21 displays this phenomenon for the low wind tercile on the left and the high wind tercile on the right. Again, this is consistent with Painemal and Minnis (2012).

In the JJA low wind tercile, the precipitation susceptibility seems to reach a maximum at intermediate LWP values and then level off at high LWP. Interestingly, in the JJA high wind tercile where the droplet number concentration is higher, the precipitation susceptibility reaches a maximum at high LWP where it appears to have reached an inflection point. This may signify the beginning of the transition from autoconversion to accretion, where the precipitation process is sufficient enough that the precipitation is less sensitive to changes in droplet concentration, leading to a decrease in precipitation susceptibility beyond the inflection point. It may be, in this particular case, that in the low wind tercile, the autoconversion mechanism dominates the precipitation process whereas the high wind tercile exhibits a possible transition from autoconversion to accretion.

However, in the winter months, the roll-over in precipitation susceptibility is apparent in both the low and high surface wind terciles. In this case, the mean cloud droplet number concentration is much lower than during the summer, which may imply a
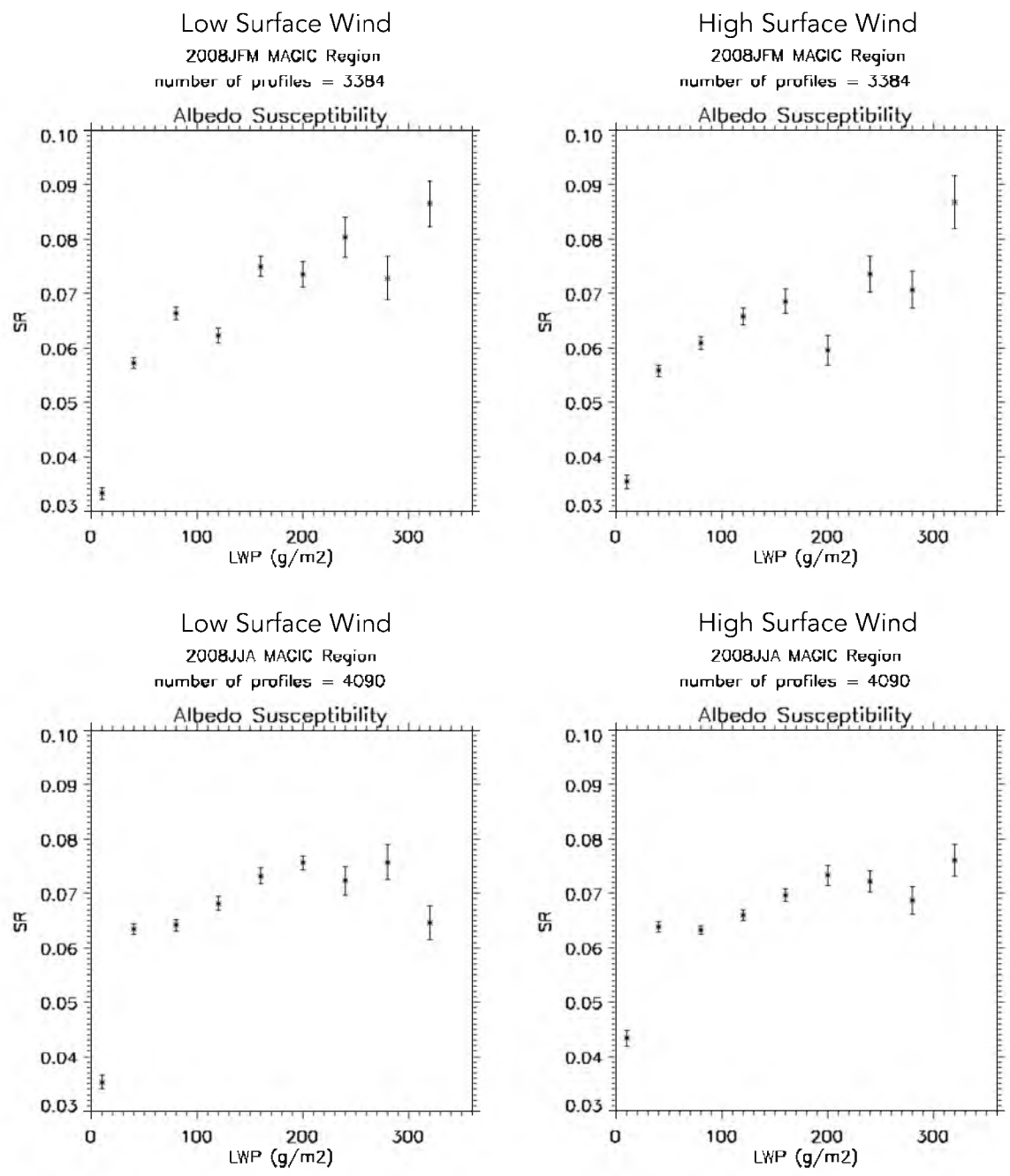
Figure 21. Albedo susceptibility for JFM (top) and JJA (bottom) for the low surface wind tercile (left) and the high surface wind tercile (right) for the MAGIC region using A-Train data.

more effective precipitation development because of the small number concentration. In addition, the difference in the mean number concentration between the low and high wind tercile in the winter is small, which may be why we see the roll-over in both surface wind conditions. It is possible that we do not see a roll-over in the summer low wind tercile precipitation susceptibility because it still has a higher mean droplet number concentration than what we see in the winter case, which may suppress efficient precipitation.

4.2 Southern Oceans Region Using A-Train Data

Taking the study further, we investigated albedo and precipitation susceptibility of marine boundary layer clouds in the southern oceans, a region dominated by a background state of boundary layer clouds (Mace 2010). The seasonal comparison of the co-dependence of albedo and precipitation susceptibility between summer and winter months, displayed in Figures 22 and 23, respectively, produced similar results to the MAGIC transect region. In the winter months (JJA), the precipitation susceptibility exhibited the same roll-over at intermediate and high LWP values, indicating a transition from autoconversion to accretion. On the other hand, the summer months (JFM) precipitation susceptibility was monotonic, characteristic of an autoconversion-dominated regime. The albedo susceptibility remained fairly consistent between the two seasons.

Furthermore, the cloud microphysical properties remained consistent with the results in the MAGIC region. The winter months were characterized by a mean droplet concentration of 9.3 cm^{-3} whereas the summer months had a mean value of 95 cm^{-3}. A study by Boers et al. (1998) compared the microphysical properties of stratocumulus clouds over the southern ocean between winter and summer using observations from the

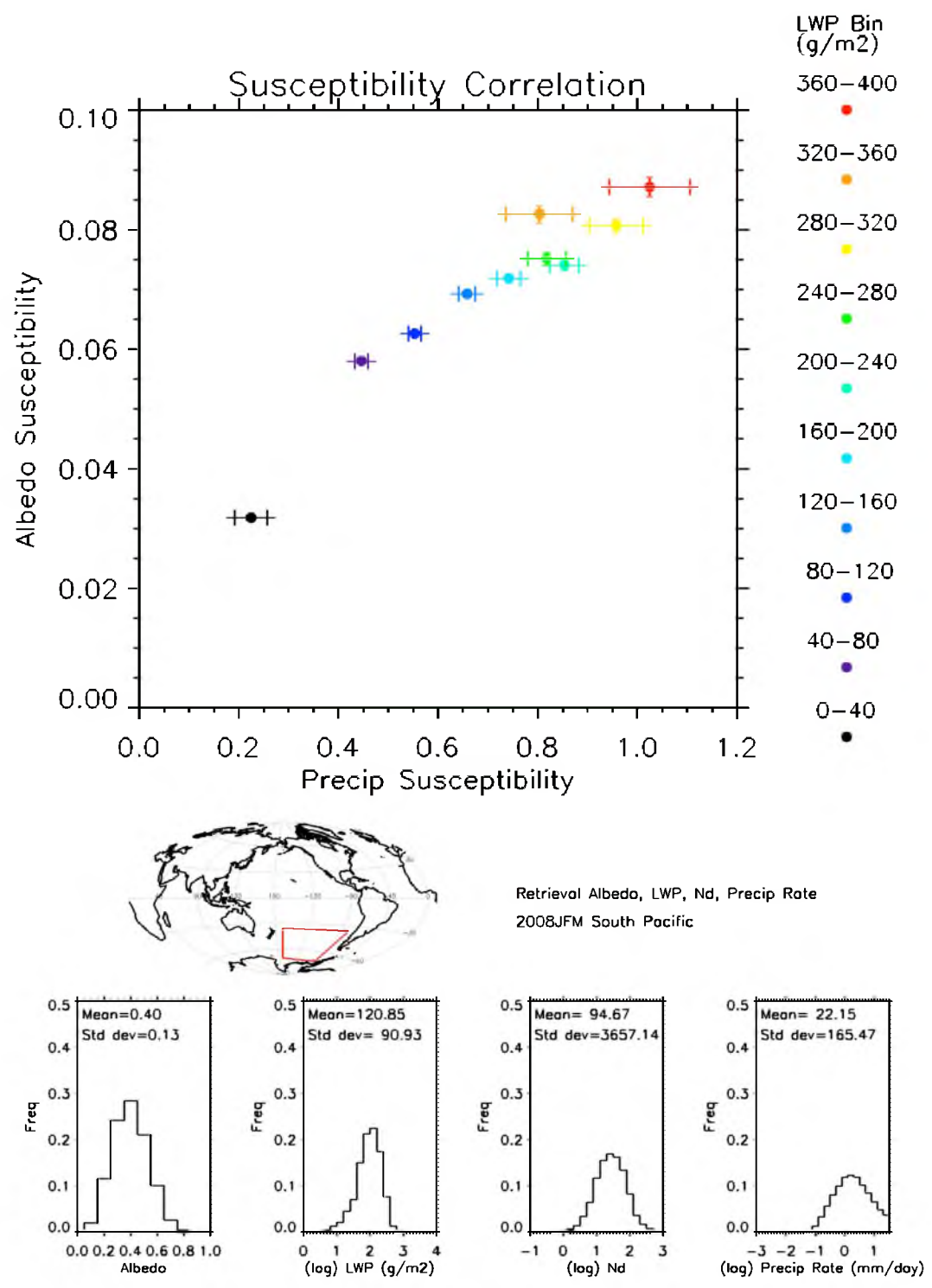Figure 22. Relationship between albedo and precipitation susceptibility for the Southern Ocean region during JFM 2008 using A-Train data.
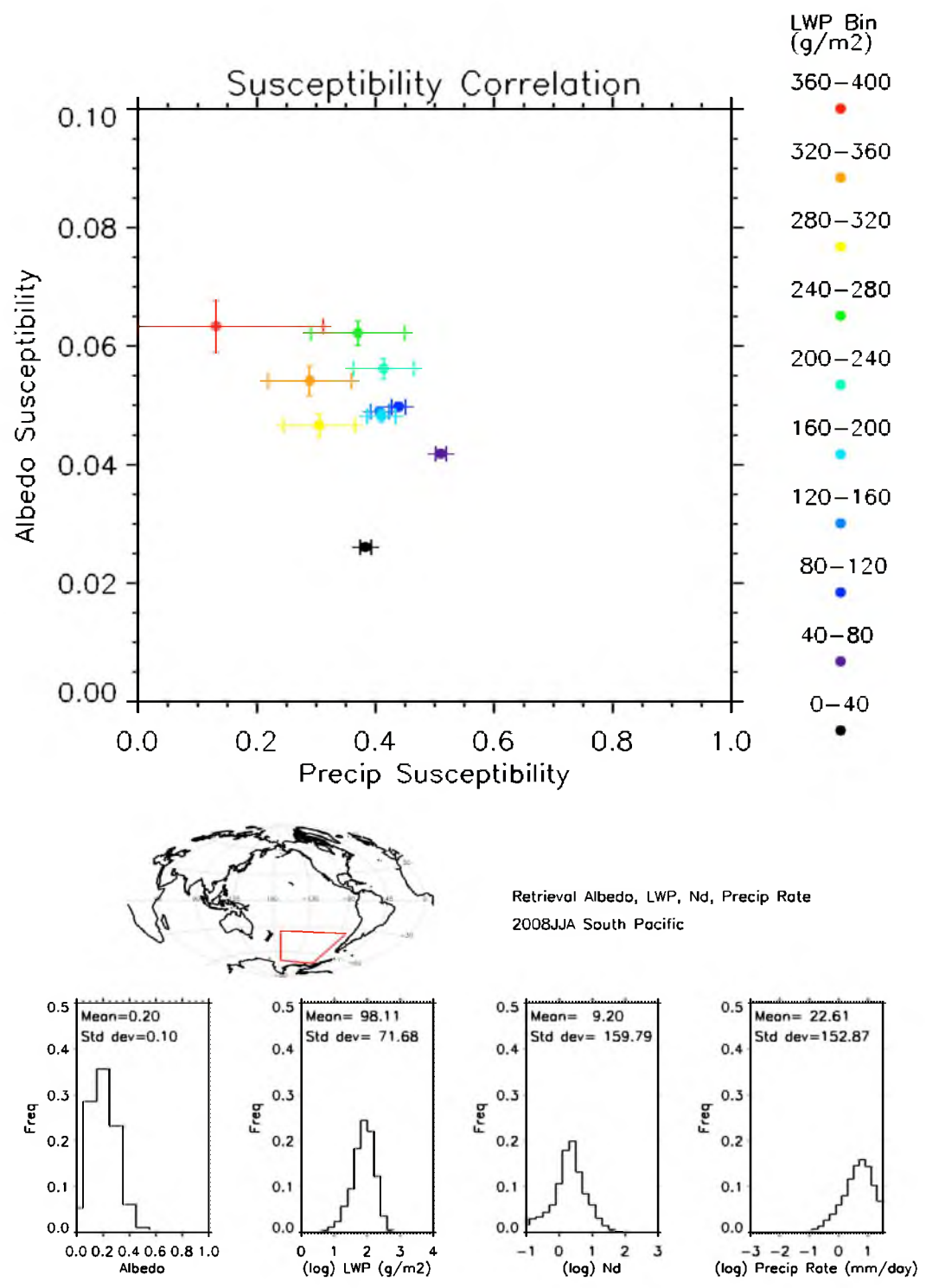
Figure 23. Same as in Figure 22 except for JJA 2008.

Southern Ocean Cloud Experiment (SOCEX). Similarly, they found the cloud droplet concentration to be higher in the summer than in the winter ranging from 35 cm^{-3} in the winter to 94 cm^{-3} in the summer.

The susceptibilities divided into low wind and high wind terciles are shown in Figure 24 for JFM and Figure 25 for JJA. Again, the high wind tercile has a larger mean droplet number concentration than the low wind tercile, and the precipitation and albedo susceptibilities followed similar patterns as in the MAGIC case. Most noticeably in the southern ocean winter high wind tercile is the roll-over in the precipitation susceptibility. This reaffirms the suggestion of an autoconversion to accretion transition occurring in the presence of higher surface winds.

4.3 ARM Retrieval Case Studies Using MAGIC Data

We used the ARM retrieval algorithm using data from the MAGIC field campaign to consider two case studies, one from the trade cumulus cloud regime and the other from the stratocumulus cloud regime. The first case study, presented in Figure 26, occurred on 11 July 2013 at 20-21 UTC in the trade cumulus regime of the MAGIC transect near Hawaii. As Figure 26 shows, these clouds were characterized by a LWP ~ 100 g m^{-2}, rain rates as high as 0.5 mm hr^{-1}, cloud mode effective radius around 20 μm, and cloud mode droplet concentrations reaching 350 cm^{-3}.

The second case study looked at the stratocumulus cloud regime near California on 21 July 2013 at 19-20 UTC, as displayed in Figure 27. In this case, the clouds were characterized by a LWP ~ 30 g m^{-2}, slight rain rates at about 0.01 mm hr^{-1}, cloud mode effective radius 10 μm or less, and cloud mode droplet concentrations greater than 1000 cm^{-3}. These two cases represent the extremes along the MAGIC transect where the
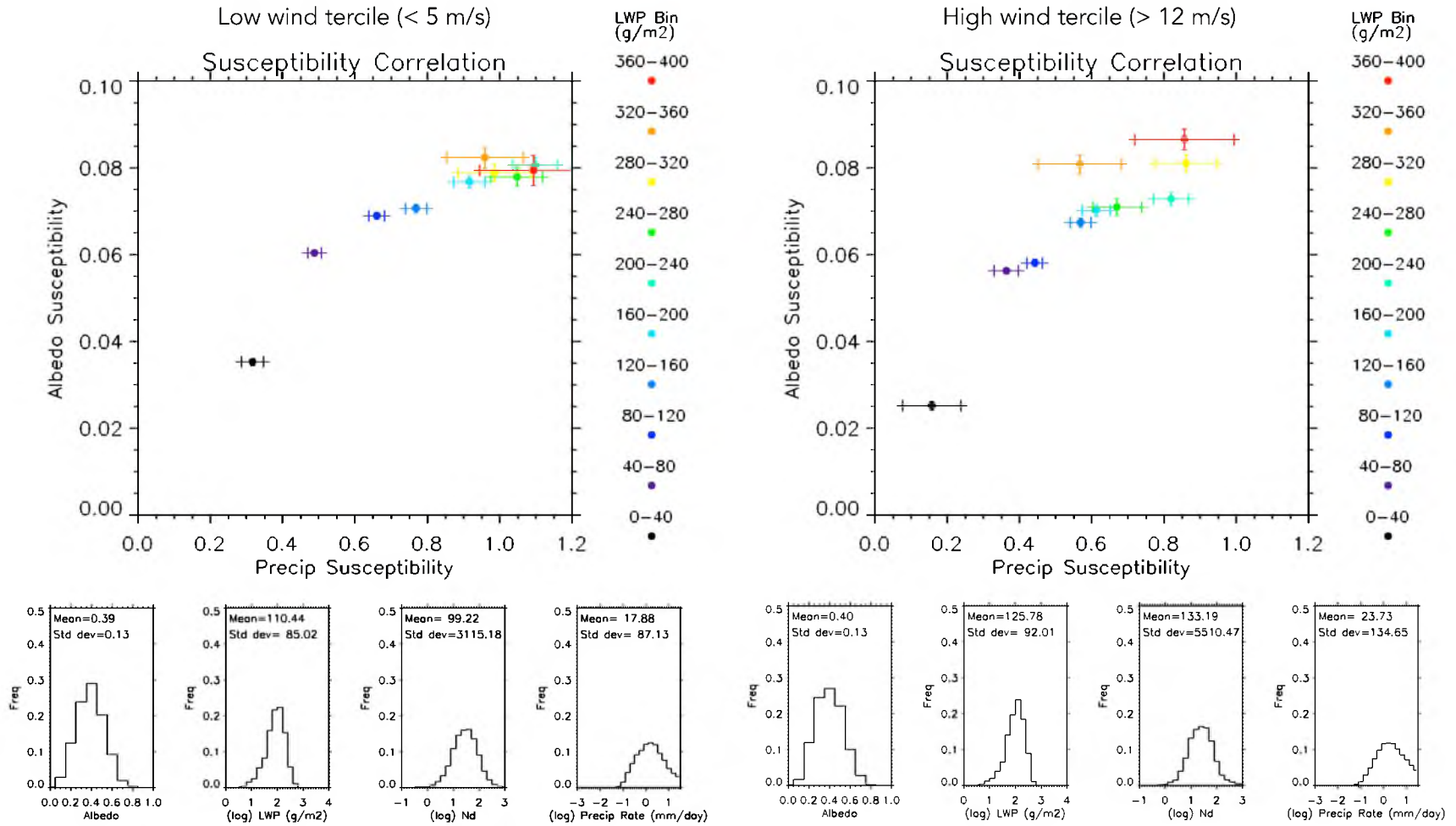
Figure 24. Susceptibility correlation divided into low surface wind conditions (left) and high surface wind conditions (right) for the Southern Ocean region during JFM 2008 using A-Train data.

Figure 25. Same as in Figure 24 except for JJA 2008.

2008JJA South Pacific Number of Profiles = 3715

High wind tercile (> 10 m/s)

Susceptibility Correlation

LWP Bin (g/m2)

360-400
320-360
280-320
240-280
200-240
160-200
120-160
80-120
40-80
0-40
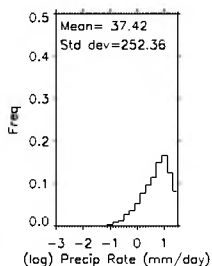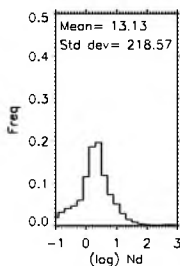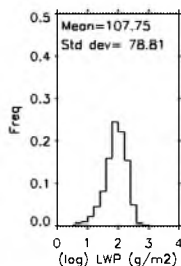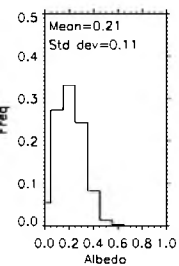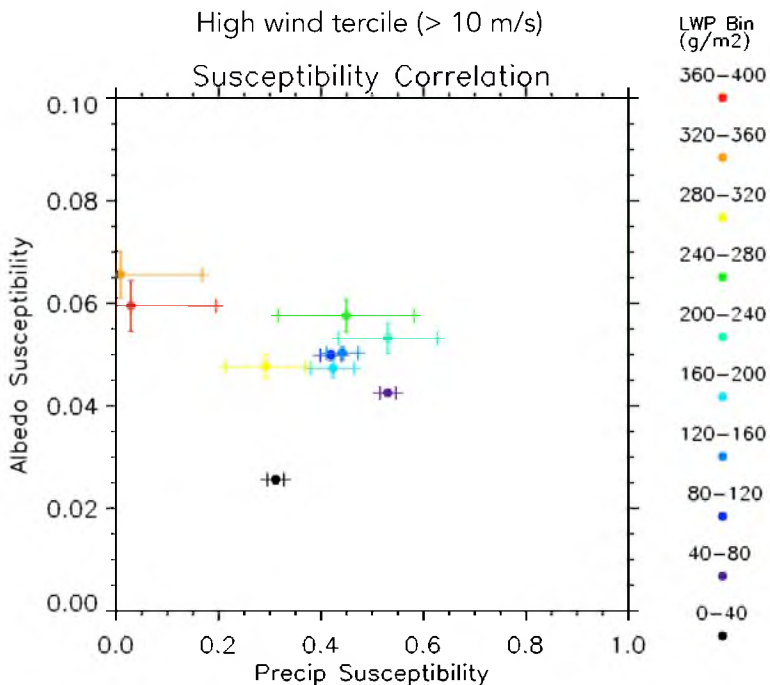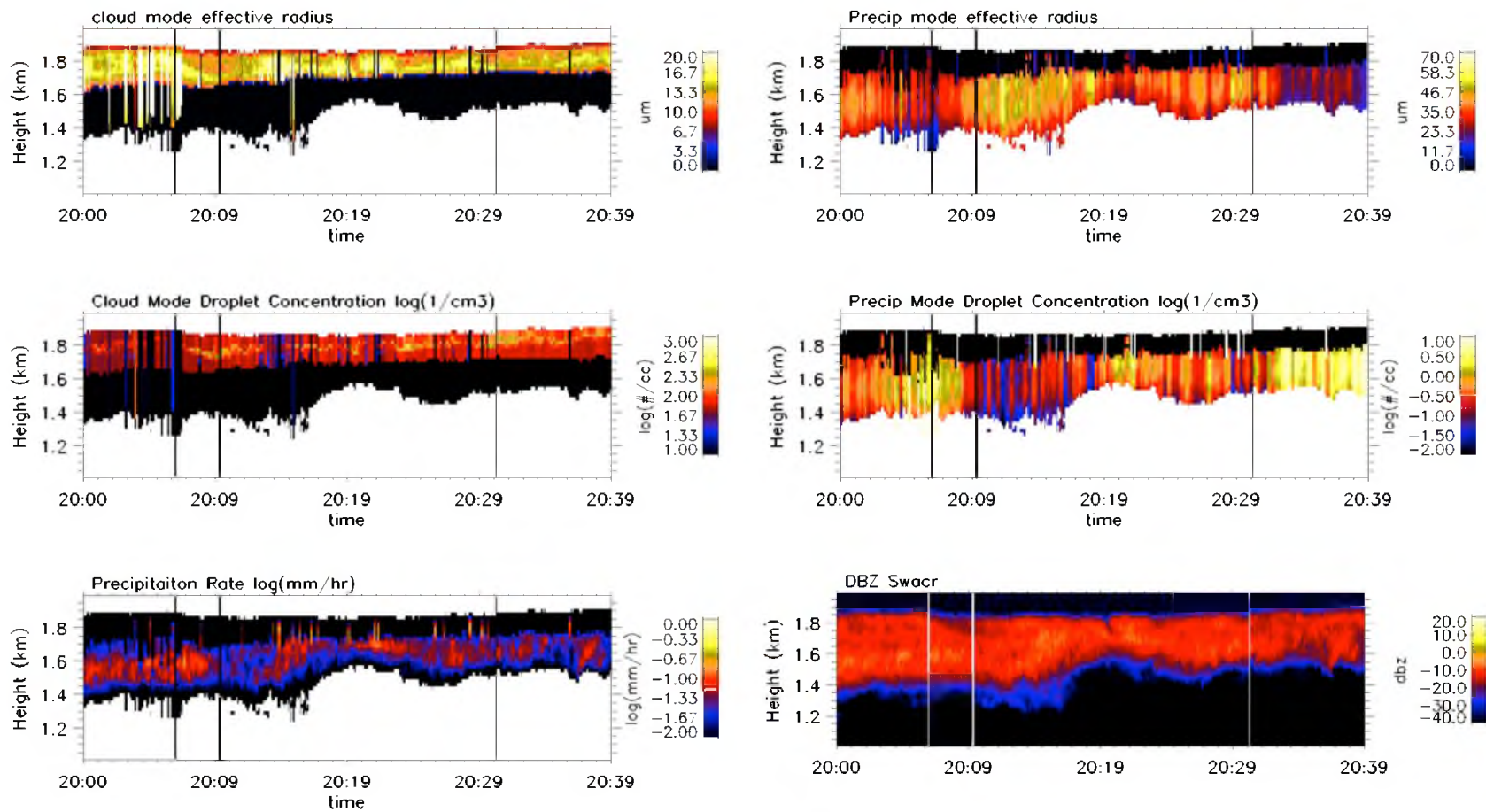
Figure 26. Retrieved cloud properties from MAGIC case study 2013 July 11 20-21 UTC using data from the MAGIC field campaign. This is a case study from the trade cumulus regime of the MAGIC transect near Hawaii.
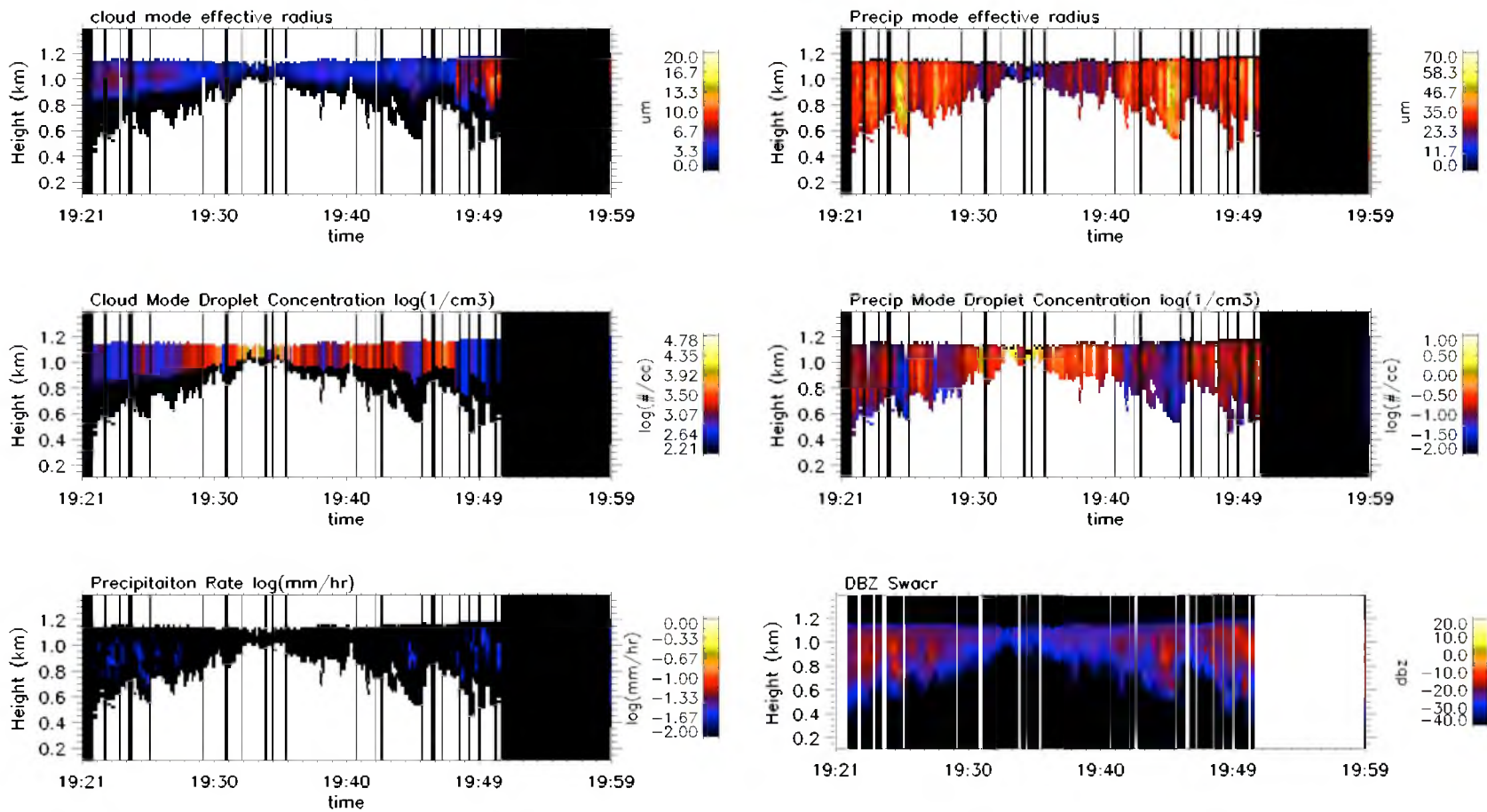
Figure 27. Retrieved cloud properties from MAGIC case study 2013 July 21 19-20 UTC using data from the MAGIC field campaign. This is a case study from the stratocumulus regime of the MAGIC transect near California.

stratocumulus clouds evolve into shallow trade cumulus. Interestingly, it may also indicate a transition from an autoconversion regime associated with the stratocumulus region to an accretion regime associated with the trade cumulus region.

We do not show susceptibility results using MAGIC data for a couple of reasons. First, the MAGIC data are still preliminary, and there may be calibration issues with the radar data because the heave motions of the ship may have interfered with radar measurements. Second, the computational time required to produce enough retrievals for a sufficient statistical sampling of cloud properties using the MAGIC data would take an unreasonable amount of time. Therefore, the two MAGIC case studies presented in this section are shown primarily to illustrate the differences in cloud properties between the stratocumulus and trade cumulus marine boundary layer cloud regions.

CHAPTER 5

SUMMARY AND CONCLUSIONS

In summary, we have reviewed the importance of marine boundary layer clouds as they are ubiquitous and affect Earth's climate. Because of the complex nature and range of physical processes that govern these clouds, it remains a challenge to accurately represent them in climate models. Thus, there is a constant need to improve understanding of marine boundary layer cloud processes.

In this study, we have investigated the albedo and precipitation susceptibilities of these clouds using A-Train satellite data. Through a recently developed cloud retrieval algorithm, we can infer cloud properties from the satellite measurements. Consistent with previous studies, we have found that precipitation susceptibility is non-monotonic with respect to LWP, and that albedo susceptibility increases or levels off with increasing LWP (Sorooshian et al. 2009, Painemal and Minnis 2012).

In an attempt to further distinguish physical controls on the cloud susceptibilities, we compared results from summer months and winter months. It was found that the summer months are characterized by larger cloud droplet number concentrations than during the winter. This seasonal variation in droplet number concentration could be due to seasonal cycles in dimethyl sulfide (DMS) production, which is emitted over the oceans by phytoplankton, and act as CCN. Indeed, DMS concentrations are higher

during the summer months (Boers et al. 1998), which may explain the increased cloud droplet number concentration during that time.

In addition, we compared the susceptibilities under high surface and low surface wind conditions. In general, cloud droplet number concentrations were larger under high surface winds, and smaller in low surface winds. It may be that more sea salt is being lofted and thus available for cloud droplet activation in higher surface winds, contributing to the larger cloud droplet number concentration under these conditions (O'Dowd et al. 1997, Feingold et al. 1999). Moreover, sea salt may be considered giant CCN (GCCN) if their radii are greater than 5 μm (Feingold et al. 1999). In their study, Feingold et al. (1999) found that at higher CCN concentrations, the addition of GCCN have the greatest potential (compared to GCCN added to low CCN concentration) for enhancing the collection process within a cloud, enabling a nonprecipitating stratocumulus into a precipitating state. Thus, it may be that the roll-over seen in the precipitation susceptibility under high wind conditions is due to an enhancement of precipitation because of the GCCN, allowing for a transition from autoconversion to accretion.

Furthermore, regarding precipitation susceptibility, cloud environments dominated by autoconversion are sensitive to N_d. The susceptibility values are higher, and there is no obvious transition into an accretion regime. Conversely, cloud environments dominated by accretion are less sensitive to N_d, and transition rapidly to lower susceptibility, indicating that the precipitation process is already efficient.

In conclusion, we have identified at least three conditions that may be potential drivers of precipitation susceptibility, and thus affect the autoconversion and accretion processes. First is the seasonal variation of cloud droplet number concentration, possibly

due to the seasonal cycle of DMS aerosol production. Second is the difference in droplet number concentration brought on by varying surface wind conditions. Third, as portrayed from the MAGIC case studies using the ARM retrieval, is an apparent transition from an autoconversion to an accretion regime associated with the stratocumulus-to-cumulus transition.

Albedo susceptibility, on the other hand, exhibited less variation than the precipitation susceptibility. Our results follow Painemal and Minnis (2012) in that albedo susceptibility under high droplet concentration conditions levels off with increasing LWP, whereas under low droplet concentrations, albedo susceptibility continues to monotonically increase. In the future, it would be interesting to investigate other meteorological controls that may affect cloud albedo and precipitation susceptibility.

REFERENCES

Abdul-Razzak, H., and S. J. Ghan, 2000: A parameterization of aerosol activation: 2. Multiple aerosol types. *J. Geophys. Res.*, **105 (D5)**, 6837–6844.

Ackerman, A. S., and Coauthors, 2009: Large-eddy simulations of a drizzling, stratocumulus-topped marine boundary layer. *Mon. Wea. Rev.*, **137**, 1083–1110.

Albrecht, B. A., 1989: Aerosols, cloud microphysics, and fractional cloudiness. *Science*, **245**, 1227–1230.

——, D. A. Randall, and S. Nicholls, 1988: Observations of marine stratocumulus clouds during FIRE. *Bull. Amer. Meteor. Soc.*, **69**, 618–626.

——, C. S. Bretherton, D. Johnson, W. H. Schubert, and A. S. Frisch, 1995: The Atlantic stratocumulus transition experiment—ASTEX. *Bull. Amer. Meteor. Soc.*, **76**, 889–904.

American Meteorological Society, cited 2014: AMS Glossary of Meteorology, Accretion. [Available online at http://glossary.ametsoc.org/wiki/Accretion].

——, cited 2014: AMS Glossary of Meteorology, Autoconversion. [Available online at http://glossary.ametsoc.org/wiki/Autoconversion].

Austin, P., Y. Wang, V. Kujala, and R. Pincus, 1995: Precipitation in stratocumulus clouds: Observational and modeling results. *J. Atmos. Sci.*, **52**, 2329–2352.

Baker, M. B., 1997: Cloud microphysics and climate. *Science*, **276**, 1072–1078.

Boers, R., J. B. Jensen, and P. B. Krummel, 1998: Microphysical and short-wave radiative structure of stratocumulus clouds over the Southern Ocean: Summer results and seasonal differences. *Quart. J. Roy. Meteor. Soc.*, **124**, 151–168.

Bohren, C. F., 1987: Multiple scattering of light and some of its observable consequences. *Amer. J. Phys.*, **55**, 524–533.

——, and D. R. Huffman, 1998: *Absorption and Scattering of Light by Small Particles.* Wiley-VCH, 544 pp.

——, and E. E. Clothiaux, 2006: *Fundamentals of Atmospheric Radiation: An Introduction with 400 Problems.* Wiley-VCH, 490 pp.

Bony, S., and J.-L. Dufresne, 2005: Marine boundary layer clouds at the heart of tropical cloud feedback uncertainties in climate models, *Geophys. Res. Lett.*, **32**, L20806.

——, and Coauthors, 2006: How well do we understand and evaluate climate change feedback processes? *J. Climate*, **19**, 3445–3482.

Boucher, O., and Coauthors, 2013: Clouds and aerosols. *Climate Change 2013: The Physical Science Basis. Contribution of Working Group I to the Fifth Assessment Report of the Intergovernmental Panel on Climate Change*, Stocker, T. F., D. Qin, G.-K. Plattner, M. Tignor, S. K. Allen, J. Boschung, A. Nauels, Y. Xia, V. Bex, and P.M. Midgley, Ed. Cambridge University Press, 571–657.

Brenguier, J.-L., H. Pawlowska, L. Schüller, R. Preusker, J. Fischer, and Y. Fouquart, 2000: Radiative properties of boundary layer clouds: Droplet effective radius versus number concentration. *J. Atmos. Sci.*, **57**, 803–821.

Bretherton, C. S., and M. C. Wyant, 1997: Moisture transport, lower-tropospheric stability, and decoupling of cloud-topped boundary layers. *J. Atmos. Sci.*, **54**, 148–167.

——, and Coauthors, 2004: The EPIC 2001 stratocumulus study. *Bull. Amer. Meteor. Soc.*, **85**, 967–977.

——, and D. L. Hartmann, 2009: Large-scale controls on cloudiness. *Clouds in the Perturbed Climate System: Their Relationship to Energy Balance, Atmospheric Dynamics, and Precipitation*, J. Heintzenburg, and R. J. Charlson, Ed., MIT Press, 217–234

Brient, F., and S. Bony 2012: How may low-cloud radiative properties simulated in the current climate influence low-cloud feedbacks under global warming?, *Geophys. Res. Lett.*, **39**, L20807.

Christi, M., and P. Gabriel, 2003: *Radiant 2.0: A User's Guide.* Colorado State University, 33 pp.

Comstock, K. K., R. Wood, S. E. Yuter, and C. S. Bretherton, 2004: Reflectivity and rain rate in and below drizzling stratocumulus. *Quart. J. Roy. Meteor. Soc.*, **130**, 2891–2918.

——, C. S. Bretherton, and S. E. Yuter, 2005: Mesoscale variability and drizzle in southeast Pacific stratocumulus. *J. Atmos. Sci.* **62**, 3792–3807.

Feingold, G., W. R. Cotton, B. Stevens, and A. S. Frisch, 1996: The relationship between drop in-cloud residence time and drizzle production in numerically simulated stratocumulus clouds. *J. Atmos. Sci.*, **53**, 1108–1122.

——, W. R. Cotton, S. M. Kreidenweis, and J. T. Davis, 1999: The impact of giant cloud condensation nuclei on drizzle formation in stratocumulus: Implications for cloud radiative properties. *J. Atmos. Sci.*, **56**, 4100–4117.

——, A. McComiskey, D. Rosenfeld, and A. Sorooshian 2013: On the relationship between cloud contact time and precipitation susceptibility to aerosol. *J. Geophys. Res. Atmos.*, **118**, 10,544–10,554.

Flato, G., and Coauthors, 2013: Evaluation of climate models. *Climate Change 2013: The Physical Science Basis. Contribution of Working Group I to the Fifth Assessment Report of the Intergovernmental Panel on Climate Change*, Stocker, T. F., D. Qin, G.-K. Plattner, M. Tignor, S. K. Allen, J. Boschung, A. Nauels, Y. Xia, V. Bex, and P.M. Midgley, Ed. Cambridge University Press, 741–866.

Frisch, A. S., G. Feingold, C. W. Fairall, T. Uttal, and J. B. Snider, 1998: On cloud radar and microwave radiometer measurements of stratus cloud liquid water profiles. *J. Geophys. Res.*, **103,** 23195–23197.

Grandey, B. S., A. Gururaj, P. Stier, and T. M. Wagner, 2014: Rainfall–aerosol relationships explained by wet scavenging and humidity. *Geophys. Res. Lett.*, doi: 10.1002/2014GL060958.

Guibert, S., J. R. Snider, and J.-L. Brenguier, 2003: Aerosol activation in marine stratocumulus clouds: 1. Measurement validation for a closure study, *J. Geophys. Res.*, **108**, 8628

Hartmann, D. L., M. E. Ockert-Bell, and M. L. Michelsen, 1992: The effect of cloud type on earth's energy balance: Global analysis. *J. Climate*, **5**, 1281–1304.

Hobbs, P. V., 1993: Aerosol-Cloud Interactions. *Aerosol-Cloud-Climate Interactions*, P.V. Hobbs, Ed., Academic Press, 33–73.

Houze, R. A., 1993: *Cloud Dynamics.* Academic Press, 573 pp.

Hu, Y. X., and K. Stamnes, 1993: An accurate parameterization of the radiative properties of water clouds suitable for use in climate models. *J. Climate*, **6**, 728–742.

Jiang, H., G. Feingold, and A. Sorooshian, 2010: Effect of aerosol on the susceptibility and efficiency of precipitation in warm trade cumulus clouds. *J. Atmos. Sci.*, **67**, 3525–3540.

Johnson, D. W., G. M. Martin, D. P. Rogers, and C. A. Friehe, 1994: Observations of the transition from stratocumulus to trade wind cumulus during ASTEX. *Proc. Eighth Conf. on Atmospheric Radiation*, Nashville, TN, Amer. Meteor. Soc., 138–140.

Jonas, P. R., 1996: Turbulence and cloud microphysics. *Atmos. Res.*, **40**, 283–306.

Karlsson, J., G. Svensson, S. Cardoso, J. Teixeira, and S. Paradise, 2010: Subtropical cloud-regime transitions: Boundary layer depth and cloud-top height evolution in models and observations. *J. Appl. Meteor. Climatol.*, **49**, 1845–1858.

Khain, A., M. Ovtchinnikov, M. Pinsky, A. Pokrovsky, and H. Krugliak, 2000: Notes on the state-of-the-art numerical modeling of cloud microphysics. *Atmos. Res.*, **55**, 159–224.

Klein, S. A., and D. L. Hartmann, 1993: The seasonal cycle of low stratiform clouds. *J. Climate*, **6**, 1587–1606.

Kollias, P., C. W. Fairall, P. Zuidema, J. Tomlinson, and G. A. Wick, 2004: Observations of marine stratocumulus in SE Pacific during the PACS 2003 cruise. *Geophys. Res. Lett.*, **31**, L22110.

Kostinski, A. B., 2008: Drizzle rates versus cloud depths for marine stratocumuli. *Environ. Res. Lett.*, **3**, 045019.

Krueger, S. K., G. T. McLean, and Q. Fu, 1995: Numerical simulation of the stratus-to-cumulus transition in the subtropical marine boundary layer. Part II: Boundary-layer circulation. *J. Atmos. Sci.*, **52**, 2851–2868.

Kummerow, C., W. S. Olson, and L. Giglio, 1996: A simplified scheme for obtaining precipitation and vertical hydrometeor profiles from passive microwave sensors. *IEEE Trans. Geosci. Remote Sens.*, **34**, 1213–1222.

Lebsock, M. D., and T. S. L'Ecuyer, 2011: The retrieval of warm rain from Cloudsat. *J. Geophys. Res.*, **116**, D20209.

Lenderink, G., and A. P. Siebesma, 2004: On the role of drizzle in stratocumulus and its implications for large-eddy simulation. *Quart. J. Roy. Meteor. Soc.*, **130**, 3429 – 3434.

Leon, D. C., Z. Wang, and D. Liu, 2008: Climatology of drizzle in marine boundary layer clouds based on 1 year of data from CloudSat and Cloud-Aerosol Lidar and Infrared Pathfinder Satellite Observations (CALIPSO). *J. Geophys. Res.*, **113**, D00A14.

Lewis, E. R., and W. J. Wiscombe, 2012: MAGIC: Marine ARM GPCI Investigation of Clouds Science/Implementation Plan. Report DOE/SC-ARM-12-020, 20 pp, http://www.arm.gov/publications/programdocs/doe-sc-arm-12-020.pdf?id=34

Lin, W., M. Zhang, and N. G. Loeb, 2009: Seasonal variation of the physical properties of marine boundary layer clouds off the California coast. *J. Climate*, **22**, 2624–2638.

Lohmann, U., 2009: Marine boundary layer clouds. *Surface Ocean–Lower Atmosphere Processes*, Geophysical Research Series No. 187, American Geophysical Union, 57–68.

——, and J. Feichter, 2005: Global indirect aerosol effects: A review. *Atmos. Chem. Phys.*, **5**, 715–737.

Mace, G. G., 2010: Cloud properties and radiative forcing over the maritime storm tracks of the Southern Ocean and North Atlantic derived from A-Train. *J. Geophys. Res.*, **115**, D10201.

Martin, G. M., D. W. Johnson, D. P. Rogers, P. R. Jonas, P. Minnis, and D. A. Hegg, 1995: Observations of the interaction between cumulus clouds and warm stratocumulus clouds in the marine boundary layer during ASTEX. *J. Atmos. Sci.*, **52**, 2902–2922.

Mauger, G. S., and J. R. Norris, 2010: Assessing the impact of meteorological history on subtropical cloud fraction. *J. Climate*, **23**, 2926–2940.

Meador, W. E., and W. R. Weaver, 1980: Two-stream approximation to radiative transfer in planetary atmospheres: A unified description of existing methods and a new improvement. *J. Atmos. Sci.*, **37**, 630–643.

Miles, N. L., J. Verlinde, and E. E. Clothiaux, 2000: Cloud droplet distributions in low-level stratiform clouds. *J. Atmos. Sci.*, **57**, 295–311.

Myers, T. A., and J. R. Norris, 2013: Observational evidence that enhanced subsidence reduces subtropical marine boundary layer cloudiness. *J. Climate*, **26**, 7507–7524.

Nakajima, T. Y., K. Suzuki, and G. L. Stephens, 2010: Droplet growth in warm water clouds observed by the A-Train. Part I: Sensitivity analysis of the MODIS-derived cloud droplet sizes. *J. Atmos. Sci.*, **67**, 1884–1896.

Nicholls, S., 1984: The dynamics of stratocumulus: Aircraft observations and comparisons with a mixed layer model. *Quart. J. Roy. Meteor. Soc.*, **110**, 1141–1170.

Norris, J. R., 1998: Low cloud type over the ocean from surface observations. Part I: Relationship to surface meteorology and the vertical distribution of temperature and moisture. *J. Climate*, **11**, 369–382.

O'Dowd, C.D., M. H. Smith, I. E. Consterdine, and J. A. Lowe, 1997: Marine aerosol, sea-salt, and the marine sulphur cycle: A short review. *Atmos. Environ.*, **31**, 73–80.

Paluch, I. R., and D. H. Lenschow, 1991: Stratiform cloud formation in the marine boundary layer. *J. Atmos. Sci.*, **48**, 2141–2158.

——, D. H. Lenschow, S. Siems, G. L. Kok, R. D. Schillawski, and S. McKeen, 1994: Evolution of the subtropical marine boundary layer: Comparison of soundings over the Eastern Pacific from FIRE and HaRP. *J. Atmos. Sci.*, **51**, 1465–1479.

Painemal, D., and P. Minnis 2012: On the dependence of albedo on cloud microphysics over marine stratocumulus clouds regimes determined from Clouds and the Earth's Radiant Energy System (CERES) data. *J. Geophys. Res.*, **117**, D06203.

Partain, P., 2007: Cloudsat MODIS-AUX auxiliary data process description and interface control document algorithm version 5.1., MODIS-AUX_PDCID_5.1, 20 pp, http://www.cloudsat.cira.colostate.edu/dataICDlist.php?go=list&path=/MODIS-AUX

Petty, G. W., 2006: *A First Course in Atmospheric Radiation.* Sundog Publishing, 459 pp.

——, and W. Huang, 2011: The modified gamma size distribution applied to inhomogeneous and nonspherical particles: Key relationships and conversions. *J. Atmos. Sci.*, **68**, 1460–1473.

Platnick, S., and S. Twomey, 1994: Determining the susceptibility of cloud albedo to changes in droplet concentration with the Advanced Very High Resolution Radiometer. *J. Appl. Meteor.*, **33**, 334–347.

Posselt, D. J., and G. G. Mace, 2014: MCMC-based assessment of the error characteristics of a combined radar-passive microwave cloud property retrieval. *J. Appl. Meteor. Clim.*, Accepted.

Randall, D., M. Khairoutdinov, A. Arakawa, and W. Grabowski, 2003: Breaking the cloud parameterization deadlock. *Bull. Amer. Meteor. Soc.*, **84**, 1547–1564.

Rodgers, C. D., 2000: *Inverse Methods For Atmospheric Sounding Theory and Practice.* World Scientific Publishing, 238 pp.

Rogers, R. R., and M.K. Yau, 1989: *A Short Course in Cloud Physics.* Pergamon Press, 293 pp.

Rosenfeld, D., 1999: TRMM observed first direct evidence of smoke from forest fires inhibiting rainfall. *Geophys. Res. Lett.,* **95,** 3105–3108.

Rotstayn, L. D., and Y. Liu, 2005: A smaller global estimate of the second indirect aerosol effect. *Geophys. Res. Lett.,* **32,** L05708.

Sandu, I., and B. Stevens, 2011: On the factors modulating the stratocumulus to cumulus transitions. *J. Atmos. Sci.,* **68,** 1865–1881.

——, ——, and R. Pincus, 2010: On the transitions in marine boundary layer cloudiness. *Atmos. Chem. Phys. Discuss.,* **10,** 2377–2391.

Savic-Jovcic, V., and B. Stevens, 2008: The structure and mesoscale organization of precipitating stratocumulus. *J. Atmos. Sci.,* **65,** 1587–1605.

Siebesma, A., and Coauthors, 2004: Cloud representation in general-circulation models over the northern Pacific Ocean: A EUROCS intercomparison study. *Quart. J. Roy. Meteor. Soc.,* **130,** 3245–3267.

Slingo, A., 1989: A GCM parameterization for the shortwave radiative properties of water clouds. *J. Atmos. Sci.,* **46,** 1419–1427.

——, and H. M. Schrecker, 1982: On the shortwave radiative properties of stratiform water clouds. *Quart. J. Roy. Meteor. Soc.,* **108,** 407–426.

Soden, B. J., and G. A. Vecchi, 2011: The vertical distribution of cloud feedback in coupled ocean-atmosphere models. *Geophys. Res. Lett.,* **38,** L12704.

Sorooshian, A., G. Feingold, M. Lebsock, H. Jiang, and G. Stephens, 2009: On the precipitation susceptibility of clouds to aerosol perturbations. *Geophys. Res. Lett.,* **36,** L13803.

Stephens, G. L., 1994, *Remote Sensing of the Lower Atmosphere: An Introduction.* Oxford University Press Inc., 544 pp.

——, 2005: Cloud feedbacks in the climate system: A critical review. *J. Climate,* **18,** 237–273.

——, and J. M. Haynes, 2007: Near global observations of the warm rain coalescence process. *Geophys. Res. Lett.,* **34,** L20805.

——, and Coauthors, 2008: CloudSat mission: Performance and early science after the first year of operation. *J. Geophys. Res.,* **113,** D00A18.

Stevens, B., and G. Feingold, 2009: Untangling aerosol effects on clouds and precipitation in a buffered system. *Nature*, **461**, (7264), 607–613.

——, and Coauthors, 2003: Dynamics and chemistry of marine stratocumulus—DYCOMS-II. *Bull. Amer. Meteor. Soc.*, **84**, 579–593.

——, W. R. Cotton, G. Feingold, and C.-H. Moeng, 1998: Large-eddy simulations of strongly precipitating, shallow, stratocumulus-topped boundary layers. *J. Atmos. Sci.*, **55**, 3616–3638.

——, G. Vali, K. Comstock, R. Wood, M. C. Van Zanten, P. H. Austin, C. S. Bretherton, and D. H. Lenschow, 2005: Pockets of open cells and drizzle in marine stratocumulus. *Bull. Amer. Meteor. Soc.*, **86**, 51–57.

Suzuki, K., and G. L. Stephens, 2009: Relationship between radar reflectivity and the time scale of warm rain formation in a global cloud-resolving model. *Atmos. Res.*, **92**, 411–419.

Teixeira, J., and Coauthors, 2011: Tropical and subtropical cloud transitions in weather and climate prediction models: The GCSS/WGNE Pacific Cross-section Intercomparison (GPCI). *J. Climate*, **24**, 5223–5256.

Terai, C. R., R. Wood, D. C. Leon, and P. Zuidema, 2012: Does precipitation susceptibility vary with increasing cloud thickness in marine stratocumulus? *Atmos. Chem. Phys.*, **12**, 4567–4583.

Twomey, S., 1977: The influence of pollution on the shortwave albedo of clouds. *J. Atmos. Sci.*, **34**, 1149–1152.

Wallace, J. M., and P. V. Hobbs, 2006: *Atmospheric Science: An Introductory Survey.* Elsevier, 438 pp.

Wang, H., and G. Feingold, 2009: Modeling mesoscale cellular structures and drizzle in marine stratocumulus. Part I: Impact of drizzle on the formation and evolution of open cells. *J. Atmos. Sci.*, **66**, 3237–3256.

Wang, M., and Coauthors, 2012: Constraining cloud lifetime effects of aerosols using A-Train satellite observations. *Geophys. Res. Lett.*, **39**, L15709.

Wang, Q., and D. H. Lenschow, 1995: An observational study of the role of penetrating cumulus in a marine stratocumulus-topped boundary layer. *J. Atmos. Sci.*, **52**, 2778–2787.

West, T. K., 2014: Using a bimodal size distribution to retrieve marine low cloud properties using A-Train satellite and ground data. M.S. thesis, Dept. of Atmospheric Science, University of Utah, 98 pp.

Wood, R., 2005: Drizzle in stratiform boundary layer clouds. Part II: Microphysical aspects. *J. Atmos. Sci.*, **62**, 3034–3050.

——, 2006: Rate of loss of cloud droplets by coalescence in warm clouds. *J. Geophys. Res.*, **111**, D21205.

——, 2012: Stratocumulus clouds. *Mon. Wea. Rev.* **140**, 2373–2423.

——, and C. S. Bretherton, 2006: On the relationship between stratiform low cloud cover and lower-tropospheric stability. *J. Climate*, **19**, 6425–6432.

Wyant, M. C., C. S. Bretherton, and P. N. Blossey, 2009: Subtropical low cloud response to a warmer climate in a superparameterized climate model. Part I: Regime sorting and physical mechanisms. *J. Adv. Model. Earth Syst.*, **1**, 7.

——, C. S. Bretherton, H. A. Rand, and D. E. Stevens, 1997: Numerical simulations and a conceptual model of the stratocumulus to trade cumulus transition. *J. Atmos. Sci.*, **54**, 168–192.

Xiao, H., C.-M. Wu, and C. R. Mechoso, 2010: Buoyancy reversal, decoupling and the transition from stratocumulus to shallow cumulus topped marine boundary layers. *Climate Dyn.*, **37**, 971–984.

Xu, H., S.-P. Xie, and Y. Wang, 2005: Subseasonal variability of the Southeast Pacific stratus cloud deck. *J. Climate*, **18**, 131–142.